Eur. Phys. J. Plus (2025) 140:378
https://doi.org/10.1140/epjp/s13360-025-06303-2

THE EUROPEAN PHYSICAL JOURNAL PLUS

Regular Article

Cross-section measurements of (α, γ) reactions on zinc isotopes using the 4π γ-summing method for astrophysics applications

S. Harissopulos[1,a], **G. Provatas**[2], **V. Foteinou**[3], **M. Axiotis**[1], **H.-W. Becker**[3], **A. Lagoyannis**[1], **E. Vagena**[1], **P. Dimitriou**[4]

[1] TANDEM Laboratory, Institute of Nuclear and Particle Physics, NCSR "Demokritos", 153.10 Aghia Paraskevi, Athens, Greece
[2] Rujer Bošković Institute, Bijenička Cesta 54, Zagreb 10000, Croatia
[3] RUBION, Ruhr-Universität Bochum, Universitätsstraße 150, 44801 Bochum, Germany
[4] Nuclear Data Section, NAPC, IAEA, Wagramer Straße 5, PO Box 100, 1400 Vienna, Austria

Received: 31 January 2025 / Accepted: 5 April 2025

Abstract The cross sections of the (α, γ) reactions on ^{64}Zn, ^{66}Zn, and ^{68}Zn were measured using the 4π γ-summing method at center-of-mass energies relevant to the p-process nucleosynthesis, ranging from 4.756 to 9.352 MeV, with isotopically enriched targets. The paper also reports the analysis procedure for the current and previous measurements, through which the uncertainty of the absolute efficiency of the employed 4π γ-summing NaI(Tl) detector was significantly reduced to ≈4%. This allowed for testing existing global models of the α-particle-nucleus optical model potential with increased sensitivity. The experimental cross-section data and resulting astrophysical S factors were compared with corresponding statistical model calculations performed using version 2.0 of the nuclear reaction code TALYS. The conclusions drawn from this comparison are presented and discussed. Additionally, the reaction rates of the three reactions investigated were calculated and compared with well-established and widely used reaction-rate databases.

1 Introduction - Motivation

In 2007, the 4π γ-summing method was reported for the first time [1] as a new technique for measuring capture reaction cross sections relevant to nuclear astrophysics, particularly for the p-process [2–4]. This method was developed jointly by the nuclear astrophysics groups at NCSR "Demokritos" in Athens, Greece, and Ruhr-Universität Bochum in Germany, inspired by our earlier experimental work [5] using an eightfold segmented large-volume NaI(Tl) scintillator detector to measure the cross section of the ^{89}Y$(p, \gamma)^{90}$Zr reaction. The 4π γ-summing method has since been successfully applied in numerous cross-section measurements of (p, γ) and (α, γ) reactions (see, e.g., [6–12]) using a NaI(Tl) *single*-crystal detector, with a cylindrical shape measuring 12 inches in length and diameter, and a borehole of 35 mm diameter along its axis. The setup used in these measurements is described in detail in Refs. [1] and [8].

The 4π γ-summing method for measuring capture reaction cross sections was adopted in 2013 by A. Simon et al. [13], who used a composite eightfold segmented NaI(Tl) detector, also cylindrically shaped (16 in. × Ø16 in.). Six years later, another γ-summing spectrometer comprising 16 separate NaI(Tl) segments assembled into a 16-inch cube was reported [14]. After 20 years of development and experimental experience since the initial measurements by Tsagkari et al. [5], the 4π γ-summing method is now considered a well-established technique for measuring capture reaction cross sections in astrophysics.

The main advantage of the 4π γ-summing method lies in the large volume of the NaI(Tl) crystal and its long decay time t_D (≈ 250 ns), which prevents the detector from distinguishing individual photons forming a γ cascade when they are emitted from excited states with mean lifetimes shorter than t_D. Consequently, the γ spectrum measured with the NaI(Tl) detector typically contains a single peak, known as the *sum peak*, which results from the summation of all aforementioned γ rays. As a result, the sum peak energy E_Σ equals the sum of the Q value of the reaction under investigation and the center-of-mass energy of the reactants, i.e.,

$$E_\Sigma = E_{c.m.} + Q. \tag{1}$$

Additionally, the cross section σ of a capture reaction can be determined using a simple formula that includes the absolute efficiency ε of the sum peak. This efficiency depends strongly on the multiplicity of the summed γ cascades, which is almost always unknown, making ε challenging to derive in most cases.

[a] e-mail: sharisop@inp.demokritos.gr (corresponding author)

Published online: 11 May 2025

In [1], we introduced a simple procedure called the "in-out method", which enabled us to derive "average multiplicities" $\langle M \rangle$ for sum peaks at different beam energies. Concurrently, we performed GEANT4 simulations to obtain the efficiencies ε of sum peaks at varying energies E_Σ and average multiplicities $\langle M \rangle$. However, due to limited experimental data, the uncertainty in ε was relatively large, ranging from 15 to 20%. Consequently, almost all relative errors in our cross-section data measured using the 4π γ-summing method, whether reported as preliminary or final, are generally around 20% or higher.

This paper reports on additional experiments conducted to reduce the uncertainties in ε to approximately 4%. It also presents new cross-section data for (α, γ) reactions on ^{64}Zn, ^{66}Zn, and ^{68}Zn. With these significantly reduced uncertainties, the paper aims to test existing global models of the α-particle–nucleus optical model potential (henceforth α-OMP) with increased sensitivity. Testing α-OMP models is crucial in nuclear astrophysics, as their predictions are used by statistical model codes based on Hauser-Feshbach (HF) theory [15].

Statistical model calculations are extensively used to calculate cross sections of nuclear reactions and their reaction rates. In the case of the p-process [2–4], the relevant reactions form a vast nuclear reaction network comprising over 20000 reactions and involving nearly 2000 nuclei with atomic numbers Z ranging from 32 to 83 (see, e.g., Fig. 4 in [8]). The reactions entering the network are neutron, proton, α-particle photodisintegrations, their competing capture reactions, as well as electron captures and β decays.

The p-process network is assumed to function at stellar temperatures ranging from ≈1.8 to 3.3 billion degrees, corresponding to explosive stellar environments like type II supernovae (SN II) [2], either just before or during their explosion. In such an environment, a class of 35 stable proton-rich nuclei, referred to as p-nuclei, are produced. These are heavier than iron, with the lightest being ^{74}Se and the heaviest ^{196}Hg (see also Fig. 2 in [8]), and cannot be synthesized by the two neutron capture processes known as the s- and r- processes, through which nuclei heavier than iron are also synthesized.

A key feature of the p-nuclei is their abundances; these are 10 to 1000 times smaller than those of the other isotopes of the same element. Since their abundances cannot be identified in stellar spectra, p-nuclei have, to date, not been observed outside the solar system. Solving the p-process network is necessary to reproduce the solar system abundances of p-nuclei. To achieve this task, various astrophysical scenarios and mathematical approaches have been proposed, some of which claim to be capable of reproducing the majority of these abundances with uncertainties smaller than a factor of 3 for essentially all p-isotopes (see, e.g., [16, 17]).

Due to the large number of reactions involved in abundance calculations, these calculations must rely almost completely on the reaction cross-section predictions of the Hauser-Feshbach (HF) theory [15]. It is therefore of key importance, in addition to any improvements in astrophysical models, to investigate the uncertainties in the nuclear data, particularly in the nuclear level densities (NLD), photon strength functions (PSF), proton/neutron- and α-particle-nucleus optical model potentials, henceforth abbreviated as p/n-OMP and α-OMP, respectively.

In a recent publication, S. Goriely et al. [18] discussed uncertainties in the aforementioned nuclear data affecting p-process abundance calculations. According to this paper, the uncertainties stemming particularly from the α-OMP propagate directly into the determination of the (α, γ) reaction rate and its reverse photodisintegration. Depending on the mass region, the production of p-nuclei may vary significantly, often exceeding even a factor of 10.

Although the significant discrepancies between observed solar system p-nuclei abundances and predicted ones are, to date, mainly attributed to uncertainties in the pure astrophysics modeling of the p-process, the nuclear physics uncertainties associated with α-capture reaction rates are still quite large and could decisively affect the abundance patterns. These uncertainties are largely due to our poor knowledge of the α-OMP at low energies. Therefore, more reliable global α-OMP models are necessary, and consequently, more data on reaction cross sections are required to constrain the associated model parameters. These needs have strongly motivated the work reported in this paper.

Nevertheless, the major challenge in the study of the p-nuclei is to determine their origin, which remains one of the most puzzling tasks to be addressed by any model of heavy-element nucleosynthesis. Understanding the origin of the p-nuclei and reproducing their solar system abundances is of paramount scientific importance. It not only helps us explain the nuclide composition of the solar system, the only galactic location where p-nuclei have been observed, but also deepens our fundamental understanding of its formation, which remains incomplete in many aspects.

2 Experiments

The experiments conducted in this work included cross-section measurements using the 4π γ-summing method [1, 8] and Rutherford backscattering spectrometry (RBS) [19] to determine the target thicknesses ξ. The γ-summing measurements were carried out at the Central Unit for Ion Beams and Radionuclides (RUBION) at Ruhr-University Bochum, Germany, using its 4-MV Dynamitron tandem accelerator. For these measurements, we utilized the most recent energy calibration of the Dynamitron accelerator reported in [20]. Based on the relative error in the analyzing magnet's constant and the beam ripple specified therein, the relative uncertainty in the energy of the incident beams from the Dynamitron accelerator was 0.13%. The RBS measurements were performed at the Tandem Accelerator Laboratory of NCSR "Demokritos" in Athens, Greece, where the uncertainty in the beam energies was ≈6 keV.

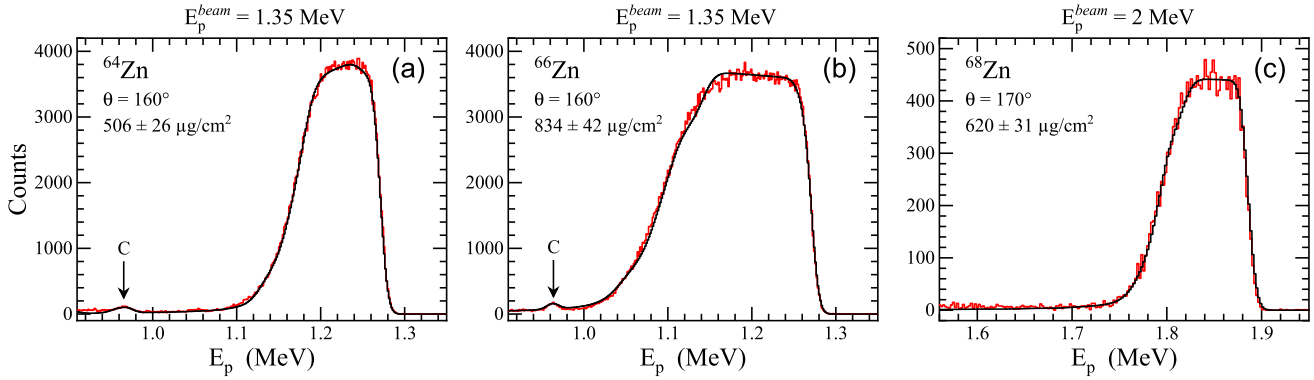

Fig. 1 Typical RBS spectra (in red), measured after the cross-section measurements. The corresponding SIMNRA calculations are depicted in black (see text for details)

2.1 RBS measurements

All targets used in the present work were self-supporting and prepared by rolling the corresponding target material. They were mounted between two thin, hollow aluminum frames, each with dimensions of ≈1×2 cm and a hole of ≈0.7×1.4 cm. Their isotopic enrichment was taken from the corresponding certificates provided by the isotope supplier.

The number of atoms per unit area and the resulting areal densities ξ of the targets were determined both before and after the cross-section experiments using Rutherford Backscattering Spectrometry (RBS) [19]. For the initial measurements, RBS spectra were measured using a deuteron beam with an energy of 1.35 MeV and the setup described in [21]. A 300-μm-thick Si surface-barrier detector was used, positioned inside the RBS chamber at a distance of approximately 15 cm from the target and at an angle of $\theta = 150°$ relative to the beam direction.

For the RBS experiments conducted after the cross-section measurements, we used the same setup but with proton beams. For the ^{64}Zn and ^{66}Zn targets, a 1.35-MeV proton beam was used. Similarly, a 300-μm-thick Si surface-barrier detector was employed, positioned at a distance of approximately 15 cm from the target and at an angle of $\theta = 160°$ relative to the beam direction. The ^{68}Zn target was analyzed in a separate run using a 2-MeV proton beam, with the Si surface-barrier detector positioned at an angle of $\theta = 170°$.

These experiments aimed to check for potential loss of target material. The measured RBS spectra are shown in Fig. 1. To derive the target areal densities ξ from all measured RBS spectra, we used the SIMNRA software package [22]. Comparing the results from the RBS experiments conducted before and after the cross-section measurements revealed that a thin layer of carbon, likely from hydrocarbons in the beam line, was deposited on the target surfaces during the measurements. These layers, indicated by an arrow in panels (a) and (b) of Fig. 1, were extremely thin, with an areal density of at most 2 μg/cm^2. Furthermore, the comparison of the RBS spectra showed no significant deterioration of the targets within statistical errors.

The areal densities ξ of the targets used are summarized in Table 1, along with the energy losses, ΔE, which were calculated using the 2013 version of the SRIM code [23], for the lowest and highest beam energies measured for each reaction investigated. In addition to the calculated ΔE values, SRIM-2013 [23] provides a relative error for these values across a range of beam energies from 1 to 10^5 keV/amu. This error represents the average deviation of the calculated ΔE values from existing experimental data. For Zn, there is only one experimental data point within the beam energy range covered in this work, which deviates from SRIM calculations by no more than 5%. Consequently, the uncertainties in ΔE quoted in Table 1 were calculated as the square root of the sum of the squared 5% SRIM error and the squared energy loss corresponding to the uncertainty in the areal density ξ. The contribution to ΔE from the uncertainty (0.13%) in the energy E_α of the incident α beam was found to be smaller than 0.3 keV in all cases and was therefore neglected. The (α, γ) reaction on ^{68}Zn is listed twice in Table 1 because it was investigated using two targets with different thicknesses, which are also provided in the table.

2.2 Cross-section measurements

Typical γ spectra measured for the nuclear reactions investigated in this work are shown in Figs. 2, 3, and 4. Figure 2 displays, in black, the γ spectrum measured at laboratory energy E_α=5.996 MeV for the ^{68}Zn$(\alpha, \gamma)^{72}$Ge reaction. For comparison, the corresponding beam-induced background, scaled to equal acquisition time, is plotted in gray. The peak labeled Σ_0, appearing at a photon energy E_{Σ_0}=10.524 MeV, is the sum peak resulting from the summation of all γ cascades depopulating the entry state and feeding the ground state of ^{72}Ge.

The peak labeled Σ_1 at 9.833 MeV is a second sum peak, resulting from the summing of the γ cascades that deexcite the entry state and populate the first excited level of ^{72}Ge. This peak is expected, as the latter level is an isomeric state with a half-life of $T_{1/2}$=444.2 ns [24], which is longer than the decay time $t_D \approx 250$ ns of the NaI(Tl) detector. The peaks Σ_0 and Σ_1 differ in energy

Table 1 Nuclear reactions investigated in this work are listed, along with the range of incident beam energies E_α in the laboratory frame covered by the cross-section measurements. The corresponding α-beam currents i_α on target are provided in the 3rd column. The relative error in E_α is 0.13%. The isotopic enrichment of the targets and their areal density ("thickness") ξ are given in the 4th and 5th columns, respectively. The energy loss ΔE of the beam, along with its uncertainty, is presented in the last column for the lowest and highest E_α values

Reaction	E_α (MeV)	i_α (nA)	Enrichment (%)	ξ (μg/cm^2)	ΔE (keV)
^{68}Zn(α, γ)^{72}Ge	5.218– 8.028	19–149	97.1(4)	538(30)	225(17)–172(13)
^{68}Zn(α, γ)^{72}Ge	5.111– 7.706	32–138	97.1(4)	625(32)	264(19)–205(15)
^{66}Zn(α, γ)^{70}Ge	5.218–10.035	3–108	96.9(2)	830(40)	346(24)–229(16)
^{64}Zn(α, γ)^{68}Ge	5.419–10.035	3–149	99.1(1)	506(25)	207(15)–140(10)

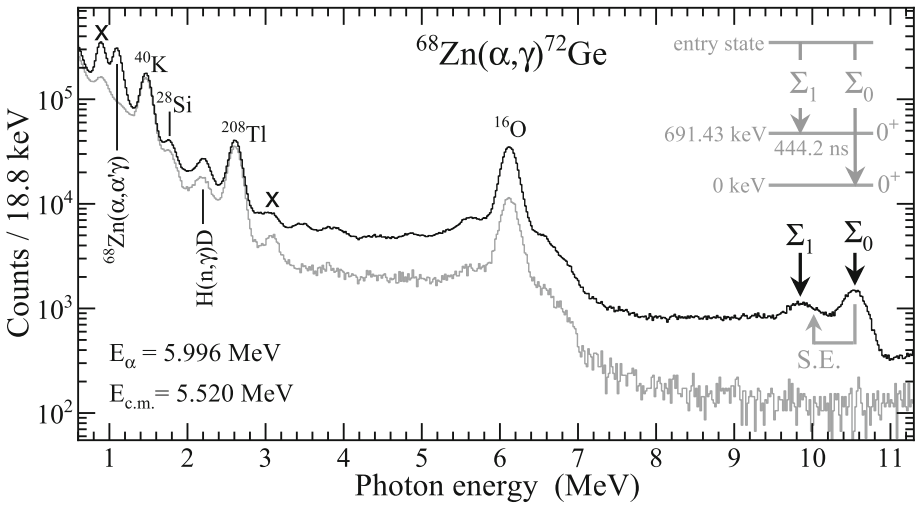

Fig. 2 Gamma spectrum, in black color, measured for the ^{68}Zn(α, γ)^{72}Ge reaction at E_α=5.996 MeV. The corresponding accumulated beam charge was 180 μQ. The relevant beam-induced background is shown by the spectrum with gray color, after being scaled to equal acquisition time. The γ peaks are explained in the text

by 691 keV, which matches the excitation energy of the aforementioned isomeric state, as indicated by the graph inserted in the top-right corner of this figure. Notably, Σ_1 exhibits a "tail" on its right side, due to the presence of the single-escape peak of Σ_0, marked as "S.E." with its location shown by the gray arrow.

The peak at ≈1.08 MeV results from the (α, $\alpha'\gamma$) reaction on ^{68}Zn, whereas the peaks labeled with ^{40}K and ^{208}Tl correspond to the well-known room background γ lines at 1.461 and 2.614 MeV, respectively. The spectrum also contains a peak at ≈2.23 MeV, stemming from the H(n, γ)D reaction, i.e., from the capture of thermalized neutrons by hydrogen present in the surrounding materials, while the neutrons are produced at different locations by the incoming beam.

The peak at ≈1.78 MeV is marked as ^{28}Si; it matches the 1.779-MeV γ-transition emitted by ^{28}Si, which is produced through the β^- decay of ^{28}Al. The ^{28}Al is formed by neutron capture on ^{27}Al, the material used for the housing of the NaI(Tl) detector. It is worth noting, however, that at 1.76 MeV, a natural background γ-transition is emitted via the β^- decay of ^{214}Bi, which is created in the decay chain of ^{238}U [25].

The peak marked as ^{16}O, together with its single-escape peak (S.E.), could also be explained as a result of the (α, $\alpha'\gamma$) reaction on ^{16}O contained in materials bombarded by the α beam on its way to the target (e.g., the oxidized surface of the beam collimators made of tantalum). The "bump" in the spectrum between ≈6.4 and 7.3 MeV is most probably due to the same reaction, involving the very short-lived ($T_{1/2}$ = 4.7 fs) excited state of ^{16}O at 6.917 MeV.

Figure 2 also contains two peaks marked as X. These peaks could not be unambiguously identified due to the low resolution of the NaI(Tl) detector. Nonetheless, they were observed in almost all (α, γ) reactions we investigated so far and are therefore considered as background lines that do not affect the cross-section measurements. Figure 2 clearly shows that above 8 MeV, where all γ lines of interest are expected, there is no peak obscuring or contaminating our sum peaks. This observation applies to all spectra measured in this work.

Typical sum peaks measured at three different α beam energies for each of the ^{66}Zn(α, γ)^{70}Ge and ^{64}Zn(α, γ)^{68}Ge reactions are shown in the left and right columns of Fig. 3, respectively. The center-of-mass energy E$_{c.m.}$, where the respective spectra were measured, along with the corresponding accumulated beam charge Q, is provided in the corresponding panels.

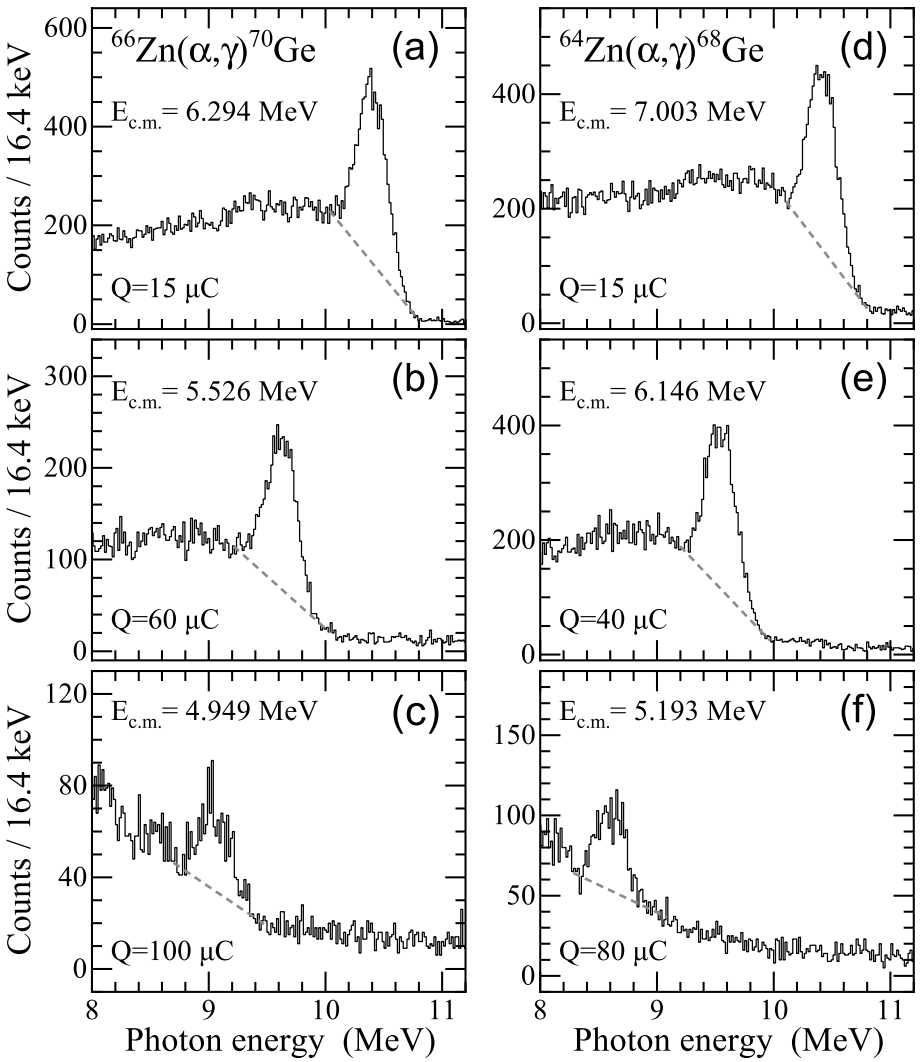

Fig. 3 Typical sum peaks measured in this work. Panels (**a**), (**b**), and (**c**) depict the sum peaks for the ^{66}Zn(α, γ)^{70}Ge reaction. The corresponding center-of-mass energies $E_{c.m.}$ and accumulated beam charges Q are also provided. Similarly, panels (**d**), (**e**), and (**f**) show the sum peaks for the ^{64}Zn(α, γ)^{68}Ge reaction. The gray dotted curves indicate the linear background below the sum peaks that was subtracted before obtaining their area I_Σ via integration or Gaussian fitting. In both reactions, the differences between the indicated center-of-mass energies equal the energy differences of the relevant sum peaks

3 Data analysis and experimental results

This subsection presents the data analysis and results from the cross-section measurements. We detail the procedures used to analyze the experimental data, particularly the efficiency calibration of the NaI(Tl) detector, and discuss the uncertainties in the determined cross sections.

First, we recall that the large volume of the NaI(Tl) detector covers almost the entire 4π solid angle around the target, which is positioned at the center of the detector along its borehole, so the detected γ transitions are already angle-integrated. Consequently, the beamtime required to measure cross sections is significantly shorter compared to the often time-demanding γ-angular distribution measurements. Secondly, due to the long decay time, t_D, of the NaI(Tl) detector, the measured γ spectrum contains the so-called sum peak, which is sufficient to determine the cross section, making the data analysis more straightforward and quicker.

In the 4π γ-summing method, the cross section σ of the capture reaction under investigation is obtained using the following equation:

$$\sigma = \frac{A}{N_A\, N_b}\, \frac{I_\Sigma}{\xi\, \varepsilon}\ , \tag{2}$$

where A is the atomic weight of the target in atomic mass units (amu), N_A is Avogadro's number, N_b is the number of beam particles, ξ is the areal density of the target (target "thickness"), I_Σ is the net area under the sum peak, and ε is the absolute efficiency of the sum peak.

I_Σ is obtained from the spectra measured with the large-volume NaI(Tl) detector, and in most cases, this is a straightforward task. However, when the cross section of interest is small, i.e., below a few μb, achieving the necessary statistics can be very time-consuming. In this work, the net area I_Σ under the sum peaks of interest and the associated (statistical) errors, were derived

by Gaussian peak fitting as well as by peak integration after subtracting a linear background under the peaks. For this purpose, the spectrum analysis codes Tv [26] and its successor hdtv [27] were used.

The uncertainty in the cross section derived from Eq. 2 also depends on the accuracy of: (a) the beam charge measurement, which enters Eq. 2 through N_b; (b) the target's areal density ξ; and (c) the absolute efficiency ε of the sum peak. N_b and ξ can be measured with very good precision, typically within 3% and 5%, respectively. This was the case in the present work. In general, the accuracy of these measurements depends on the current integrator used to measure the beam charge and the technique applied to determine ξ. The latter is usually measured using Rutherford backscattering spectrometry (RBS) [19] or X-ray fluorescence (XRF) [28]. These techniques are widely used and provide accurate results, provided that the target being analyzed does not have a "puzzling" composition. Self-supporting targets, like those used in this work, or targets made by evaporating isotopically enriched material onto a high-Z thick backing foil (such as Au, Ta, or W), with a thickness of less than 1 mg/cm^2, are typically ideal for in-beam cross-section measurements with the 4π γ-summing method.

3.1 Efficiency calibration

In contrast to I_Σ, N_b, and ξ, the absolute efficiency of the sum peak, ε, which appears in Eq. 2, is not straightforward to determine in the case of the 4π γ-summing method. Generally, a larger detector volume is expected to result in a higher ε. However, if the detector is composed of multiple crystals rather than a single one, its summing ability, and therefore ε, can decrease significantly with increasing fragmentation. This effect can be illustrated by comparing the spectrum reported in [5] for the ^{89}Y$(p,\gamma)^{90}$Zr reaction measured at 3 MeV with the spectrum provided in [7] for the same reaction at the same beam energy.

Apart from the detector's fragmentation, ε depends strongly on the multiplicity of the γ cascades summed by the NaI(Tl) detector. Since the sum peak is formed by summing many different γ cascades, each with varying multiplicity that may change with different beam energies, ε depends on the "average multiplicity", $\langle M\rangle$, of the summed γ cascades. The definition of $\langle M\rangle$ and examples can be found in [1]. Briefly, $\langle M\rangle$ is calculated by

$$\langle M\rangle = \sum_i B_i M_i \,, \tag{3}$$

where M_i is the multiplicity of the i-th γ cascade contributing to the formation of a sum peak, and B_i is the corresponding "effective cascade branching," i.e., the product of the branching ratios of all γ transitions forming this γ cascade.

As shown in [1], the ε of the NaI(Tl) detector used in that study, as well as in the present work, decreases from 0.12 to 0.08 for a 12-MeV sum peak as the multiplicity increases from 2 to 4. This was one of the findings of the "in-out method," which we first developed to derive the "average multiplicities" of sum peaks at different beam energies, as described in detail in [1].

As a first step in the in-out method, we measured sum peaks from well-studied resonances in ^{26}Mg, ^{27}Al, and ^{28}Si with well-known multiplicities. Spectra were taken with the corresponding target positioned at two different locations: at the center of the detector's borehole ("in") and at its entrance ("out"). Using the corresponding sum peak intensities I_Σ^{in} and I_Σ^{out}, we derived an empirical relation between the measured "in-out sum peak intensity ratio" R and the average multiplicity $\langle M\rangle$, given by

$$R = \frac{I_\Sigma^{in}}{I_\Sigma^{out}} = 2.48(13)^{\langle M\rangle} \,, \tag{4}$$

which is specific to the detector used. Solving for $\langle M\rangle$, we then obtain

$$\langle M\rangle = \frac{ln(R)}{ln(2.48)} = \frac{ln(R)}{1.101} \,, \tag{5}$$

In parallel, we performed GEANT4 calculations to simulate the geometry of the NaI(Tl) detector, its response to photons, and the expected sum peaks for different sum peak energies E_Σ and average multiplicities $\langle M\rangle$. More details on the latter procedure is given in [1].

The first results obtained with our in-out method are presented in Fig. 14 of Ref. [1], where ε is plotted versus different energies E_Σ of sum peaks measured for six radiative capture reactions that produce three even-even, two even-odd, and one odd-odd compound nuclei. In all cases, ε can be described by a single exponential function:

$$\varepsilon = \varepsilon_0 + \alpha \exp(-\beta/E_\Sigma). \tag{6}$$

However, the values of the coefficients ε_0, α, and β differ depending on whether the compound nucleus produced by the reaction under investigation is even-even, even-odd, or odd-odd.

Using the resulting three exponential curves, we were able to extract ε for various E_Σ values without the need to apply the in-out method to every capture reaction investigated, as these curves do not require knowledge of $\langle M\rangle$. This allowed us to analyze the experimental data not only from subsequent cross-section measurements but also from those carried out before the in-out method was first conceptualized and applied. However, due to the limited data points used to derive these exponential curves, the uncertainty in ε was comparatively higher than that of other methods, i.e., at least 15 to 20%. Consequently, almost all relative errors in our

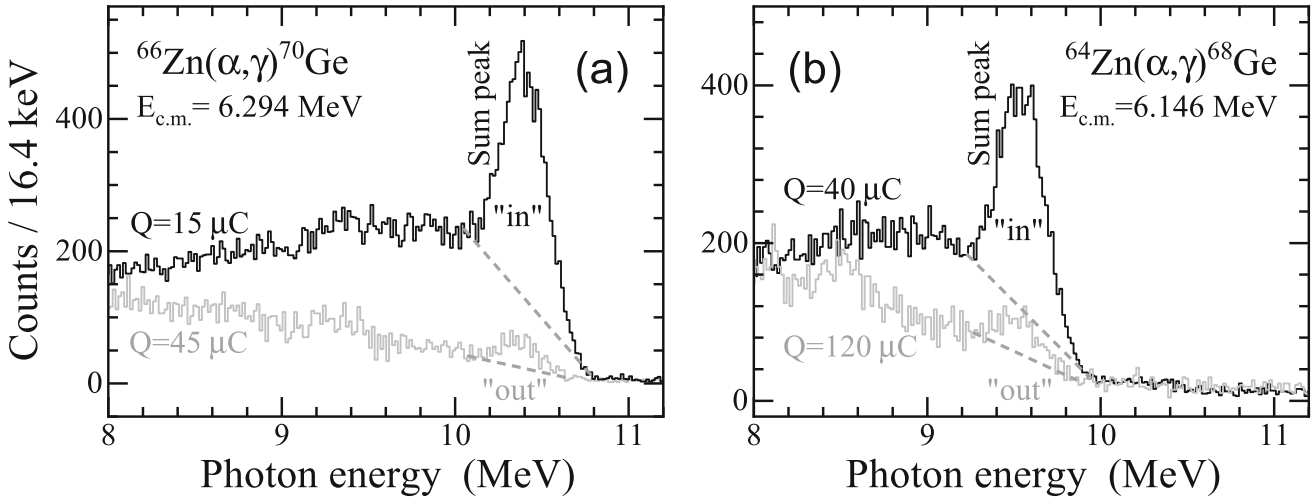

Fig. 4 Panel (**a**): "In" and "out" sum peaks measured for the ^{66}Zn(α, γ)^{70}Ge reaction at E$_{c.m.}$=6.294 MeV. Panel (**b**) depicts the "in" and "out" sum peaks for the case of the ^{64}Zn(α, γ)^{68}Ge reaction at E$_{c.m.}$=6.146 MeV. The corresponding accumulated beam charges Q are also indicated (see also text for details)

cross-section data measured with the 4π γ-summing method, whether reported as preliminary or final, are of the order of 20% or higher.

To significantly reduce the uncertainties in ε, we applied our in-out method to three more (α, γ) reactions that produce even-even compound nuclei and seven additional (p, γ) reactions leading to even-odd nuclei. The latter reactions are: ^{92}Mo(p, γ)^{93,g}Tc, ^{92}Mo(p, γ)^{93,m}Tc, ^{94}Mo(p, γ)^{95}Tc, ^{96}Mo(p, γ)^{97}Tc, ^{98}Mo(p, γ)^{99}Tc, ^{106}Pd(p, γ)^{107}Ag, and ^{116}Sn(p, γ)^{117}Sb. Experimental details of these (p, γ) reactions on the Mo isotopes, ^{106}Pd, and ^{116}Sn are given in Refs. [6, 9] and [12], respectively. The additional (α, γ) reactions are the two on ^{64}Zn and ^{66}Zn reported in this work and on ^{60}Ni. Experimental details and cross-section results for the ^{60}Ni(α, γ)^{64}Zn reaction will be presented in a forthcoming paper. Here, only the corresponding findings from the in-out method applied in this case were included.

The additional measurements allowed us to enrich our previous ε-vs.-E_Σ plots from Ref. [1] with 95 additional data points. As a result, the uncertainties in the ε values extracted by the updated exponential curves now have an average relative error of $\approx$ 4%. The present paper reports on the experimental procedures through which the additional 95 data points were obtained. Typical "in" and "out" spectra measured in this work for the ^{64}Zn(α, γ)^{68}Ge and ^{66}Zn(α, γ)^{70}Ge reactions are shown in Fig. 4.

Panels (a) and (d) of Fig. 5 depict the in-out intensity ratios R obtained using the in-out method for the capture reactions indicated therein, which produce an even-even and an even-odd compound nucleus, respectively. The ratios R are plotted versus the energy of the corresponding sum peaks measured at different beam energies. The relative errors of these ratios range from 5% to 20%. The average multiplicities $\langle M \rangle$, derived from these ratios using the detector-specific empirical relation given by Eq. 5, are plotted in panels (b) and (e). The errors in the $\langle M \rangle$ values, obtained via error propagation applied to Eq. 5, range between 6% and 9%.

The average multiplicities $\langle M \rangle$ were subsequently used to calculate the absolute sum peak efficiencies ε. This step is described here using as example the case of a sum peak of energy E_Σ=11.355 MeV and $\langle M \rangle$=3.356. For a given $\langle M \rangle$ value in decimal form Q.xyz, (e.g, 3.356), the corresponding efficiency of the NaI(Tl) detector can be calculated using

$$\varepsilon_{\langle M \rangle} = (1 - 0.xyz) \times \varepsilon_{M=Q} + 0.xyz \times \varepsilon_{M=Q+1} \tag{7}$$

Applying Eq. 7 for $\langle M \rangle$=3.356, one obtains

$$\varepsilon_{3.356} = (1 - 0.356) \times \varepsilon_{M=3} + 0.356 \times \varepsilon_{M=4} \tag{8}$$

Using the values $\varepsilon_{(M=3)} = 0.1213$ and $\varepsilon_{(M=4)} = 0.0846$ derived from Monte Carlo simulations, which are shown in Fig.10 of [1], one obtains $\varepsilon = 0.1082$. The corresponding relative error is 15.3%, which results from error propagation applied to Eq. 8, taking into account that the relative errors derived from the simulations for M=3 and M=4 are 15% and 22% respectively.

The absolute sum peak efficiencies ε corresponding to panels (b) and (d) of Fig. 5, derived as described above, are depicted in panels (c) and (f). The black curves in these panels indicate the efficiency curve obtained using Eq. 6. The gray dotted curves indicate the corresponding upper and lower efficiency values. These values were obtained through a comprehensive error analysis that accounted for the covariance of the coefficients ε_0, α, and β entering the exponential function given by Eq. 6.

It is worth emphasizing that the efficiency curves shown in black in panels (c) and (f) allow for extracting ε as a function of the sum peak energy solely, without the need to know *a priori* the multiplicity of the sum peak. These efficiency curves, which are specific to the detector used, and their uncertainties, depicted by the gray dotted curves, were used in this work to obtain the cross sections and their errors, independently of any multiplicity M.

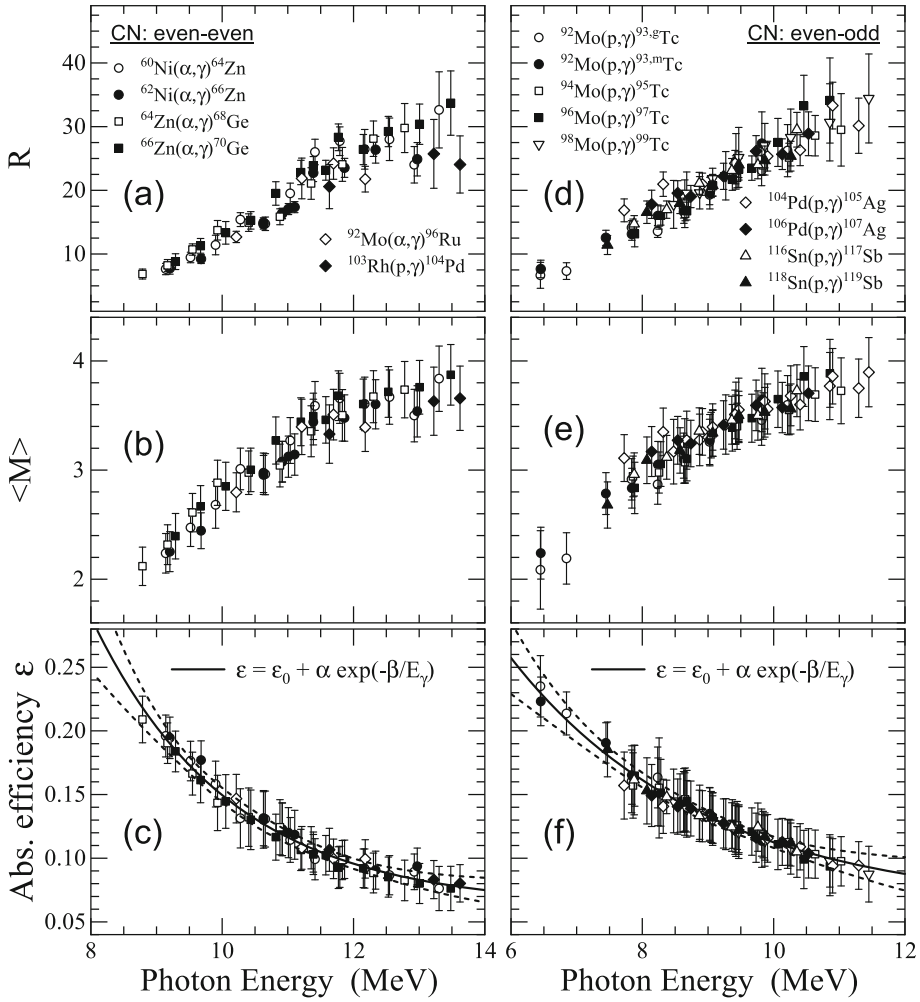

Fig. 5 Panels (**a**) and (**d**): In-out intensity ratios R measured for the indicated capture reactions producing an even-even and an even-odd compound nucleus, respectively. The corresponding average multiplicities $\langle M \rangle$ are plotted in panels (**b**) and (**e**). The resulting absolute sum peak efficiencies ε derived for each case, as described in the text, are depicted in panels (**c**) and (**f**) (see text for more details)

3.2 Cross sections and astrophysical S factors

The cross sections determined in this work and the resulting astrophysical S factors are given in Tables 2, 3, and 4. The first column in all three tables lists the α-beam energies E_α, in the laboratory system, at which γ spectra were measured for the corresponding nuclear reaction. As explained in the beginning of section 2, the relative error in E_α is 0.13%. The second column indicates the energy losses ΔE in the corresponding targets. Their uncertainties were calculated as explained in section 2.1. In all cases, the relative errors in ΔE are 7.1%. In the third column, we provide the respective center-of-mass energies $E_{c.m.}$ derived from the effective beam energies E_{eff} by

$$E_{c.m.} = E_{eff}\,\frac{m_{Zn}}{m_\alpha + m_{Zn}} = \left(E_\alpha - \frac{\Delta E}{2}\right)\frac{m_{Zn}}{m_\alpha + m_{Zn}}\ . \tag{9}$$

Hereby, the atomic masses m_{Zn} and m_α of the Zn target isotopes and the α beam, respectively, were taken by the recent atomic mass evaluation [29]. The errors in $E_{c.m.}$ given in Tables 2, 3, and 4 were calculated by taking the square root of the sum of the squares of the uncertainties in $\Delta E/2$, E_α and the energy straggling e_s of the α beam at the center of the target, with e_s calculated using the SIMNRA code [22].

The fourth column in Tables 2, 3, and 4 provides the energy E_{Σ_0} of the sum peaks calculated using Eq. 1. The quoted errors equal the errors of the corresponding center-of-mass energies $E_{c.m.}$. Notably, E_{Σ_0} also indicates at which excitation energy the compound nucleus is formed, with the associated uncertainty. The cross sections, σ, given in these tables were calculated with Eq. 2, whereas the corresponding astrophysical S factors, S, were determined by

$$S(E) = \sigma(E)\ E\ e^{2\pi\eta(E)}\ , \tag{10}$$

where $\eta(E)$ is the Sommerfeld parameter [30].

Similarly, the quoted errors in the cross sections were calculated using error propagation for Eq. 2 and the corresponding uncertainties in N_b, ξ, I_Σ and ε. As already mentioned above, the relative uncertainty in N_b, i.e., that of the measurement of the

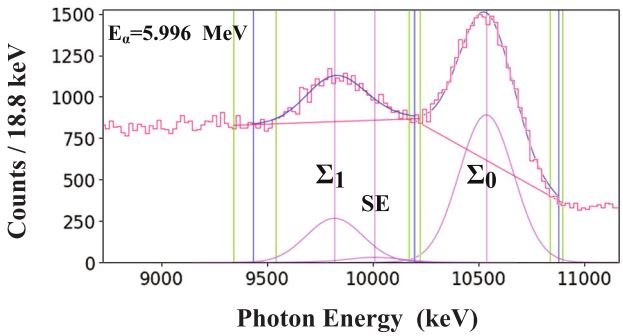

Fig. 6 Gaussian peak fitting of the sum peaks Σ_0 and Σ_1, measured at a laboratory energy of E_α=5.996 MeV for the ^{68}Zn(α, γ)^{72}Ge reaction. The single-escape peak (SE) of Σ_0 is also shown. These peaks are the same as those displayed in Fig. 2 (see also text in section 2.2 for details). The vertical green lines indicate the regions selected to determine the background below the peaks

Table 2 The total cross sections, σ_T, and the astrophysical S factors, S_T, determined in this work for the ^{64}Zn(α, γ)^{68}Ge reaction are listed in the fifth and sixth columns, respectively. The incident energy of the α beam in the laboratory system, E_α, is given in the first column, with a relative error of 0.13%. The corresponding energy loss in the target, ΔE, is provided in the second column, while the resulting center-of-mass energy, $E_{c.m.}$, is shown in the third column. The energy, E_{Σ_0}, of the corresponding sum peak is listed in the fourth column. Its uncertainty equals the error in the corresponding $E_{c.m}$

E_α (MeV)	ΔE (keV)	$E_{c.m}$ (MeV)	E_{Σ_0} (MeV)	σ_T (μb)	S_T (10^{14} MeV b)
5.419	207 ± 15	5.002 ± 0.020	8.402	1.22 ±0.22	1451 ± 266
5.619	202 ± 14	5.193 ± 0.020	8.593	3.02 ±0.43	1432 ± 204
5.820	198 ± 14	5.384 ± 0.020	8.784	5.7 ±0.66	1134 ± 131
6.021	194 ± 14	5.575 ± 0.020	8.975	12.9 ±1.2	1128 ± 106
6.221	190 ± 13	5.765 ± 0.020	9.165	22.3 ±1.9	893 ± 78
6.422	186 ± 13	5.956 ± 0.020	9.356	37.0 ±2.9	707 ± 55
6.623	183 ± 13	6.146 ± 0.020	9.546	53.8 ±3.9	507 ± 37
7.025	176 ± 12	6.528 ± 0.020	9.928	111 ±8	280 ± 21
7.526	168 ± 12	7.003 ± 0.021	10.403	199 ±15	113 ± 9
8.028	161 ± 11	7.479 ± 0.021	10.879	398 ±31	59 ± 5
8.529	155 ± 11	7.954 ± 0.021	11.354	653 ±51	28.9 ± 2.3
9.031	149 ± 11	8.429 ± 0.022	11.828	1003 ±76	14.6 ± 1.1
9.533	144 ± 10	8.903 ± 0.022	12.303	1542 ±123	8.1 ± 0.7
10.035	140 ± 10	9.378 ± 0.022	12.777	1589 ±145	3.3 ± 0.3

α-beam charge was $\approx$ 3% and the errors in ξ are given in Table 1. In the case of the ^{64}Zn(α, γ)^{68}Ge reaction, the statistical error in I_Σ at the two lowest measured center-of-mass energies, 5.193 and 5.002 MeV, was 6.8% and 14%, respectively, and $\leq$3% at higher energies. For the ^{66}Zn(α, γ)^{70}Ge reaction, the statistical error was 8.3% and 11% at $E_{\text{c.m.}} = 5.193$ and 5.002 MeV, respectively, and $\leq$2.5% at higher energies.

Concerning the ^{68}Zn(α, γ)^{72}Ge reaction, the average statistical error in I_{Σ_0} under the sum peak Σ_0 (see also Fig. 2) was 3.5%. The net area I_{Σ_1} under the second sum peak Σ_1 was obtained by simultaneously fitting two Gaussian peaks: one for Σ_1 and a second one for the single-escape (S.E.) peak of Σ_0. Notably, their energy difference is smaller than their width. Consequently, as shown in Fig. 6, the peaks are not well separated. As a result, the statistical error in I_{Σ_1} from the Gaussian fitting was significantly larger, ranging between 15% and 20%.

The values of the remaining quantity entering Eq. 2, i.e., the absolute efficiency ε of the sum peaks of interest, can be read from panel (c) of Fig. 5. The relative uncertainty in ε varies with the energy E_Σ of the sum peak. According to this panel, the largest unceratinties in ε are at sum peak energies where no data points are available, i.e., at $E_\Sigma < 8.785$ MeV and at $E_\Sigma > 13.622$ MeV. At this limits, the relative error in the fitted ε values is 7 and 11%, respectively. However, in the energy range between 9 and 12.5 MeV, where the vast majority ($\approx$90%) of the cross sections determined in this work refer to, the relative error in ε ranges from 3.6 to 4.5%.

4 Statistical model calculations

As mentioned in Sect. 1, this work is motivated by the need to test the predictions of existing global models for the α-OMP. This is crucial for accurately calculating the reaction rates of nuclear reactions involving alpha particles, which, in the case of the *p*-process,

Table 3 Same as in Table 2 but for the ^{66}Zn(α, γ)^{70}Ge reaction

E_α (MeV)	ΔE (keV)	$E_{c.m}$ (MeV)	E_{Σ_0} (MeV)	σ_T (μb)	S_T (10^{14} MeV b)
5.218	346 ±24	4.756 ±0.013	8.844	0.44 ±0.07	1926 ±295
5.419	339 ±24	4.949 ±0.013	9.037	1.19 ±0.13	1932 ±214
5.619	332 ±23	5.141 ±0.013	9.229	3.21 ±0.27	2030 ±174
5.820	325 ±23	5.334 ±0.013	9.421	6.76 ±0.53	1758 ±139
6.021	318 ±22	5.526 ±0.013	9.614	12.9 ±0.9	1454 ±109
6.221	312 ±22	5.718 ±0.013	9.806	27.4 ±1.9	1382 ±97
6.422	306 ±21	5.911 ±0.013	9.998	47.4 ±3.5	1122 ±83
6.623	300 ±21	6.102 ±0.013	10.190	83.4 ±5.9	962 ±68
6.823	294 ±20	6.294 ±0.013	10.382	141 ±10	821 ±59
7.024	289 ±20	6.486 ±0.013	10.574	208 ±15	629 ±45
7.225	284 ±20	6.678 ±0.013	10.765	340 ±24	549 ±39
7.426	279 ±19	6.869 ±0.013	10.957	459 ±32	408 ±29
7.626	274 ±19	7.061 ±0.013	11.148	651 ±46	326 ±23
7.827	269 ±19	7.252 ±0.013	11.340	850 ±59	245 ±17
8.028	265 ±18	7.443 ±0.013	11.531	1014 ±70	173 ±12
8.228	260 ±18	7.635 ±0.013	11.722	816 ±56	84 ±6
8.630	253 ±18	8.017 ±0.013	12.104	703 ±50	27.6 ±2.0
9.031	245 ±17	8.398 ±0.014	12.486	758 ±59	12.2 ±1.0
9.533	237 ±16	8.875 ±0.014	12.963	977 ±90	5.6 ±0.5
10.035	229 ±16	9.352 ±0.014	13.440	969 ±109	2.2 ±0.2

Table 4 Partial and total cross sections, σ, and astrophysical S factors, S, determined in this work for the ^{68}Zn(α, γ)^{72}Ge reaction. The subscripts g and m in the σ and S symbols refer, respectively, to the cross sections to the ground state of ^{72}Ge and to its isomeric state at an excitation energy of E_X=691.43 keV. σ_T and S_T are the resulting total cross sections and the corresponding astrophysical S factors. The quantities E_α, ΔE, $E_{c.m.}$ and E_{Σ_0} are the same as in Table 2. The first 11 lines of the table provide the results obtained with the target having a thickness ξ=625 ± 32 μg/cm^2, whereas the next 10 lines give the results obtained with the 538 ± 30-μg/cm^2-thick target

E_α (MeV)	ΔE (keV)	$E_{c.m}$ (MeV)	E_{Σ_0} (MeV)	σ_g (μb)	S_g (10^{14} MeV b)	σ_m (μb)	S_m (10^{14} MeV b)	σ_T (μb)	S_T (10^{14} MeV b)
5.469	254 ±18	5.045 ±0.022	10.049	3.09 ±0.23	3259 ±243	0.36 ±0.10	382 ±108	3.45 ±0.25	3641 ±266
5.668	248 ±18	5.235 ±0.022	10.239	6.70 ±0.49	2851 ±208	0.83 ±0.25	351 ±105	7.53 ±0.55	3203 ±233
5.767	246 ±18	5.330 ±0.022	10.334	10.5 ±0.8	2905 ±212	1.25 ±0.31	341 ±86	11.8 ±0.8	3246 ±229
5.867	243 ±17	5.425 ±0.022	10.429	16.2 ±1.2	2924 ±210	1.89 ±0.51	341 ±92	18.1 ±1.3	3266 ±229
5.966	241 ±17	5.520 ±0.022	10.524	24.9 ±1.8	2979 ±216	2.81 ±0.64	336 ±77	27.7 ±1.9	3315 ±229
6.165	236 ±17	5.710 ±0.022	10.714	42.0 ±3.1	2285 ±166	4.65 ±1.06	253 ±58	46.7 ±3.2	2537 ±176
6.264	234 ±17	5.805 ±0.022	10.809	44.2 ±3.2	1642 ±120	4.75 ±1.11	176 ±41	49.0 ±3.4	1819 ±127
6.463	229 ±16	5.995 ±0.023	10.999	31.2 ±2.3	557 ±41	2.85 ±0.94	51 ±17	34.1 ±2.5	608 ±44
6.612	226 ±16	6.138 ±0.023	11.142	29.3 ±2.2	308 ±23	3.48 ±1.02	36.7 ±10.8	32.8 ±2.4	345 ±25
7.259	213 ±15	6.754 ±0.023	11.758	20.7 ±1.6	27.2 ±2.1	2.44 ±1.06	3.2 ±1.4	23.1 ±1.9	30.4 ±2.5
7.706	205 ±15	7.181 ±0.023	12.185	33.4 ±2.5	12.2 ±0.9	4.29 ±1.33	1.6 ±0.5	37.7 ±2.8	13.8 ±1.0
5.418	220 ±16	5.013 ±0.021	10.017	2.61 ±0.25	3214 ±301	0.29 ±0.11	352 ±134	2.90 ±0.27	3566 ±330
5.619	215 ±16	5.205 ±0.021	10.209	5.91 ±0.49	2891 ±240	0.66 ±0.19	321 ±91	6.57 ±0.52	3213 ±256
5.820	211 ±16	5.397 ±0.021	10.401	13.2 ±1.1	2713 ±218	1.53 ±0.39	314 ±81	14.7 ±1.1	3027 ±233
5.848	210 ±16	5.423 ±0.021	10.427	16.4 ±1.9	2989 ±340	2.06 ±0.81	376 ±148	18.5 ±2.0	3365 ±371
6.021	206 ±15	5.588 ±0.021	10.592	30.3 ±2.4	2720 ±213	3.59 ±1.02	323 ±91	33.9 ±2.6	3043 ±232
6.221	202 ±15	5.780 ±0.021	10.784	47.7 ±3.7	1963 ±152	4.24 ±1.39	174 ±57	52.0 ±3.9	2137 ±162
6.422	198 ±15	5.971 ±0.021	10.975	41.7 ±3.2	815 ±63	4.10 ±1.15	80 ±23	45.8 ±3.4	895 ±67
7.024	187 ±14	6.545 ±0.021	11.549	21.5 ±2.2	55 ±6	2.07 ±0.83	5.3 ±2.1	23.6 ±2.4	61 ±6
7.526	179 ±13	7.023 ±0.021	12.027	29.6 ±2.7	17.2 ±1.6	4.02 ±1.41	2.3 ±0.8	33.6 ±3.1	19.5 ±1.8
8.028	172 ±13	7.500 ±0.022	12.504	59.3 ±5.4	9.0 ±0.8	5.49 ±2.02	0.8 ±0.3	64.8 ±5.8	9.8 ±0.9

Table 5 Nuclear input parameters (1st column) and corresponding phenomenological or semi-microscopic models used in our TALYS−2.0 calculations. The proton–, neutron– and alpha-particle–nucleus optical model potentials (OMPs) are indicated with *p*-OMP, *n*-OMP and α-OMP, respectively. The model notation used for discussion is given in parenthesis

Parameter	Phenomenological models	Semi-microscopic models
p/*n*-OMP	(KD): Global model of Koning and Delaroche [32]	(JLM/B): Spherical Lane-consistent model of Bauge, Delaroche and Girod [33, 34]
α-OMP	(Avr/I): α-OMP of V. Avrigeanu et al. [35]; TALYS keyword: **alphaomp 6**	(αOMP/III): Dispersive α-OMP of Demetriou et al. [36]; TALYS keyword: **alphaomp 5**
NLD	(CTFG): TALYS-specific version (see in [31]) of the Constant Temperature Fermi-Gas model of Gilbert and Cameron [37]; TALYS keyword: **ldmodel 1**	(HFB/Sk): NLDs from a combinatorial method using nuclear structure properties determined with the Hartree-Fock-Bogolyubov (HFB) model and the BSk14 Skyrme force [38, 39]; TALYS keyword: **ldmodel 5**
PSF	(SMLO): Simplified Modified Lorentzian [40–42]; for $E1$ and $M1$ transitions; TALYS keywords: **strength 9** for $E1$ transitions and **strengthM1 3** for $M1$ transitions.	(HFB/T/QRPA/G): PSFs from temperature-dependent HFB plus QRPA calculations using the D1M Gogny force [31, 43, 44]; for $E1$ and $M1$ transitions; TALYS keywords: **strength 8** for $E1$ transitions and **strengthM1 8** for $M1$ transitions.

are emitted through (γ, α) photoreactions at stellar temperatures of the order of $2-3\times10^9$ K. These reactions, along with competing (γ, p) and (γ, n) reactions, disintegrate nuclei previously synthesized by the *s*- and *r*-process, thereby producing *p*-isotopes.

These photodisintegrating reactions, along with β^+ decays, form nucleosynthetic pathways on the proton-rich side of the nuclear chart, i.e., on the "left" side of the stability valley, covering a wide mass range from ^{196}Hg down to ^{74}Se. Therefore, the reaction rates of many hundreds, if not thousands, of reactions involving α particles must be considered to perform reliable *p*-nuclei abundance calculations. Since the vast majority of these rates cannot be determined experimentally, they must be calculated using statistical model codes based on the Hauser-Feshbach theory [15].

Apart from nuclear masses, optical model potentials (OMPs) for protons, neutrons, and α-particles, along with nuclear level densities (NLDs) and photon strength functions (PSFs), are key "input parameters" in statistical model calculations. When experimental data are unavailable, the need to cover a wide mass range necessitates the use of "global" models. These models can either be phenomenological, where parameters are derived from fitting data obtained from nuclear reactions on isotopes across the broadest possible mass range, thus avoiding the need for "local" adjustments, or they can be physically sound microscopic models based on first principles. The latter additionally ensure reliable extrapolations beyond experimentally accessible regions.

In this work, we performed statistical model calculations using version 2.0 of the well-established and widely used nuclear reaction code TALYS [31], which offers a large portfolio of 28 models (for a summary, see Table VI in [12]). These include two OMP models for protons and neutrons, henceforth referred to as *p*/*n*-OMP, eight models for the α-particle-nucleus OMP (α-OMP), six different NLD models, and 12 PSF models (three for $M1$ and nine for $E1$ γ-transitions). Thus, using TALYS, 1152 model combinations are available for HF calculations. In this paper, however, we considered only the 8 models listed in Table 5. In particular, we focused on three model combinations, which, according to the model notation given in Table 5, are the following:

1. KD – Avr/I – CTFG – SMLO (for $E1$ transitions) – SMLO (for $M1$ transitions)
2. KD – α-OMP/III – HFB/Sk – HFB/T/QRPA/G (for $E1$ transitions) – HFB/T/QRPA/G (for $M1$ transitions)
3. JLM/B – α-OMP/III – HFB/Sk – HFB/T/QRPA/G (for $E1$ transitions) – HFB/T/QRPA/G (for $M1$ transitions)

The first model combination is purely phenomenological and is used by TALYS as its "default" combination. To simplify the discussion, we shorten its notation to K6193, where the letter "K" replaces KD, which represents the global proton- and neutron-OMP of Koning and Delaroche [32]. The subsequent number sequence corresponds to the numbers in the keywords used by TALYS for the sequence α-OMP – NLD – PSF(E1) – PSF(M1). These keywords are given in bold in Table 5. Specifically, 6193 denotes the α-OMP labeled as "Avr/I" in Table 5, followed by the "CTFG" NLD, the "SMLO" for $E1$ transitions, and the "SMLO" for $M1$ transitions.

Similarly, we shorten the notation of the second model combination to K5588, and by analogy, that of the third model to J5588, with "J" replacing JLM/B, i.e., the spherical Lane-consistent proton- and neutron-OMP of Bauge, Delaroche, and Girod [33, 34]. Notably, the third model combination is purely semi-microscopic. The three model combinations, K6193, J5588, and K5588, were selected for our calculations with the aim to:

- test the predictive power of a semi-microscopic model combination (J5588), comprising the only available global semi-microscopic dispersive α-OMP of Demetriou et al. [36], the currently most robust microscopic NLD model from a physics standpoint [38, 39], and the very recent microscopic PSF model [31, 43, 44] describing both $E1$ and $M1$ γ transitions.
- compare the cross sections calculated with the J5588 combination with those resulting from the extensively used phenomenological K6193, which comprises two quite successful global OMPs, namely the proton- and neutron-OMP of Koning and Delaroche [32] and the α-OMP of V. Avrigeanu et al. [35], the well-established TALYS-specific version of the Constant Temperature Fermi-Gas

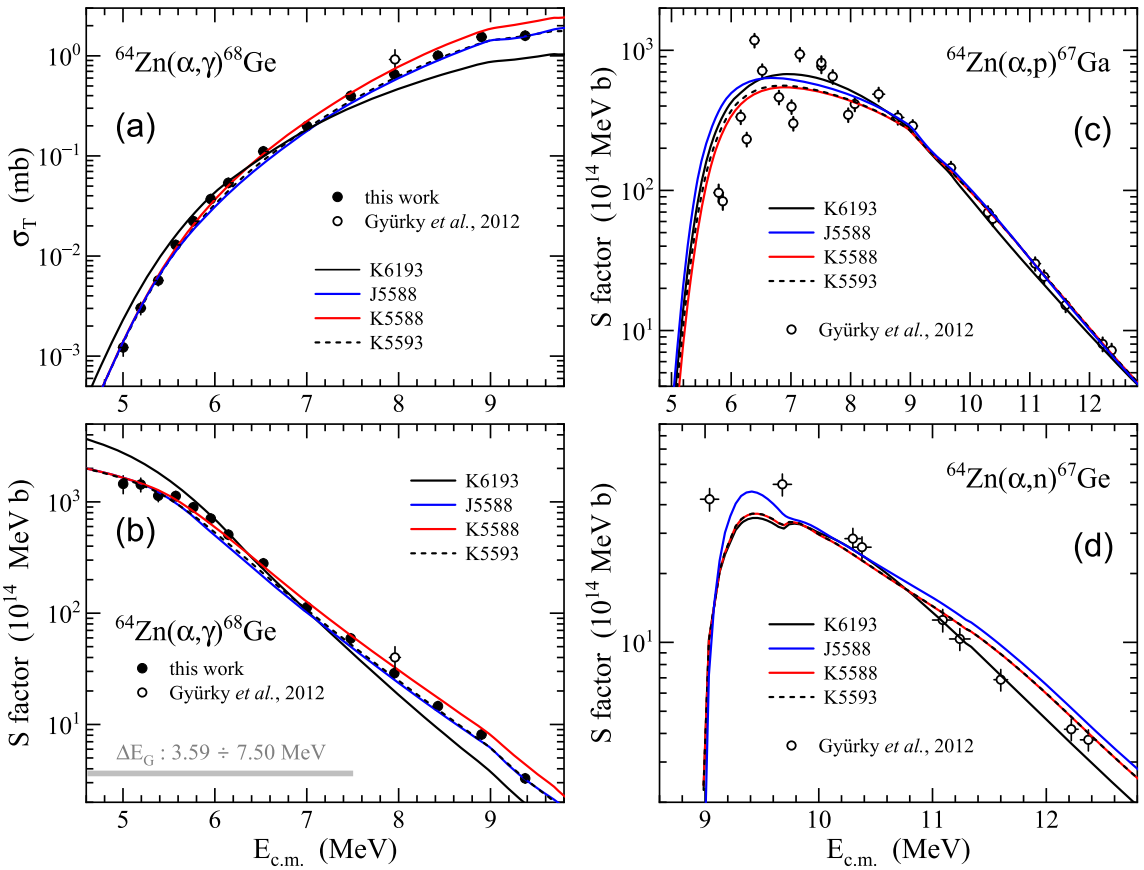

Fig. 7 Panels (**a**) and (**b**): Total cross sections and S factors, respectively, determined in this work (black solid circles) for the ^{64}Zn(α, γ)^{68}Ge reaction compared with TALYS−2.0 model combinations, as indicated in the legend by the different types of curves. The open circle was reported in [45]. The gray bar shown in panel (**b**) indicates the Gamow energy region for typical *p*-process stellar temperatures between 2 and 3 billion degrees Kelvin. Panels (**c**) and (**d**) show a comparison of the S factors reported in [45] for the ^{64}Zn(α, p)^{67}Ga and ^{64}Zn(α, n)^{67}Ge reactions, respectively (see text for more details)

model of Gilbert and Cameron (see [31]), and the only phenomenological PSF model (SMLO), developed recently [40–42] for both $E1$ and $M1$ γ transitions.

- compare the predictions of the semi-microscopic *p*-OMP of Bauge, Delaroche, and Girod [33, 34] with those of the phenomenological OMP of Koning and Delaroche [32]. This is of particular interest because the (α, p) reaction channel competes strongly with the (α, γ) one at low energies in all three reactions investigated in this work. It is worth recalling that in our recent work [11], we found that the *p*-OMP of Bauge, Delaroche, and Girod [33, 34] was equally, if not more, successful than the OMP of Koning and Delaroche [32] in reproducing the cross sections of proton capture reactions on Sr isotopes.

5 Discussion

5.1 Cross sections and astrophysical S factors

Our TALYS−2.0 calculations for the ^{64}Zn(α, γ)^{68}Ge and ^{66}Zn(α, γ)^{70}Ge reactions are compared with our experimental data in Figs. 7 and 8, respectively. In both figures, panel (a) shows the comparison of total cross sections, while the corresponding astrophysical S factors are plotted in panel (b).

In the case of ^{64}Zn(α, γ)^{68}Ge, we also include in panel (a) the cross section measured by Gy. Gyürky et al. [45] at $E_{c.m.} = 7.96$ MeV, along with the corresponding S factor in panel (b). Our experimental data for both reactions lie within the Gamow energy window, which corresponds to typical *p*-process temperatures between 2 and 3 billion degrees Kelvin. As indicated by the gray bars shown in panels (b) of Figs. 7 and 8, this window ranges from 3.59 to 7.50 MeV.

The cross sections calculated with TALYS−2.0 and the corresponding S factors are plotted in panels (a) and (b) of Figs. 7 and 8 as solid curves in different colors. The TALYS−2.0 results obtained using the K6193 (default) model combination are indicated by the solid black curves, while those derived with the J5588 and K5588 combinations are shown in blue and red, respectively.

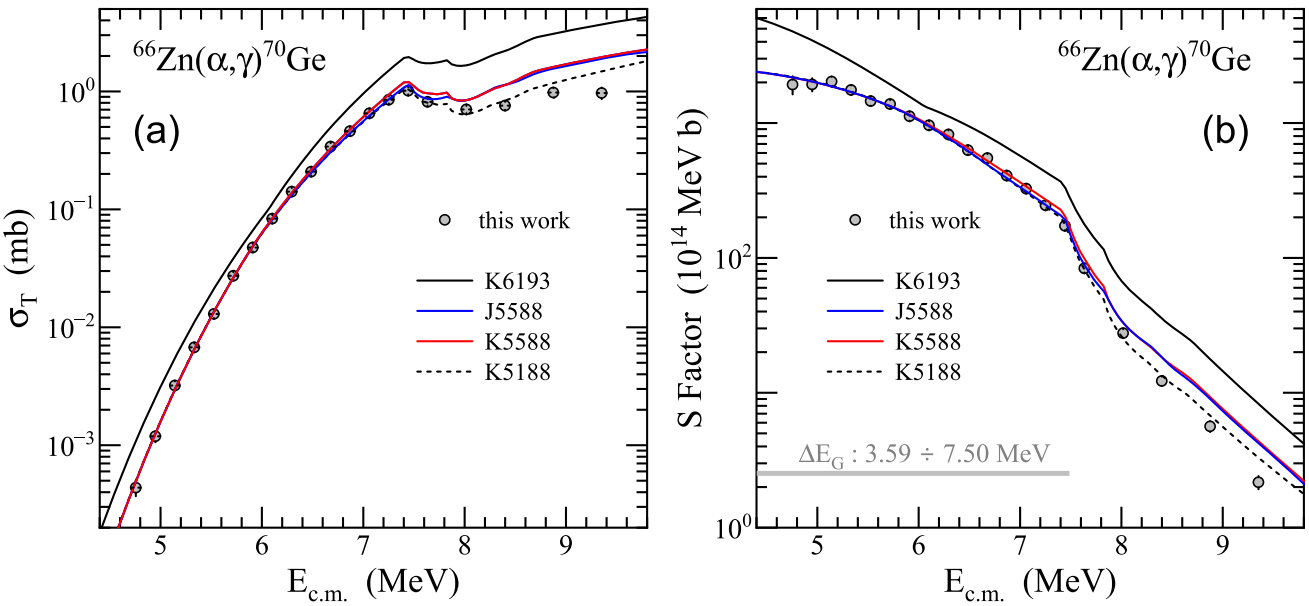

Fig. 8 Same as in Fig. 7 but for the ^{66}Zn(α, γ)^{70}Ge reaction

The black dotted curves shown in panels (a) and (b) of Fig. 7 indicate the relevant TALYS−2.0 results derived using the K5593 model combination, which includes the global phenomenological *p*/*n*-OMP of Koning and Delaroche [32], the semi-microscopic α-OMP/III of Demetriou et al. [36], the HFB/Sk NLD, and the SMLO PSF for both $E1$ and $M1$ γ transitions. This curve corresponds to TALYS−2.0 calculations with the best χ^2 obtained in a standard χ^2 analysis of the 16 possible combinations of the models listed in Table 5. It is worth noting that, in every χ^2 analysis performed in this work, the SMLO PSF model for $E1$ transitions was not allowed to be combined with the HFB/T/QRPA/G PSF for $M1$ transitions, and vice versa.

In the case of ^{66}Zn(α, γ)^{70}Ge, the analogous black dotted curve shows the TALYS−2.0 calculations obtained using the K5188 model combination, which includes the KD *p*/*n*-OMP, the TALYS-specific CTFG NLD, and the HFB/T/QRPA/G PSF for both $E1$ and $M1$ γ transitions. Notably, the curves corresponding to the best χ^2 were not obtained using a self-consistent model combination from a physics perspective; they serve only for comparison with the three combinations of interest: the default purely phenomenological K6193, the fully semi-microscopic J5588, and the K5588 model.

Independent of the standard χ^2 analysis, we also applied a "goodness-of-fit estimator" procedure by calculating the root-mean-square F_{rms}-factor, proposed by A. Koning [46, 47], for all 16 model combinations mentioned. As expected, the model combinations with the smallest χ^2 were also those with the smallest F_{rms}-values in all cases. Moreover, using this quantity, we were able to obtain a direct measure of the relative deviation of each model combination from the experimental data, as discussed in [46].

According to the F_{rms} values obtained for the ^{64}Zn(α, γ)^{68}Ge reaction, the TALYS−2.0 calculations derived using the K5593 model combination (best χ^2) deviate, on average, by 13% from the experimental data. The calculations derived using the K6193, J5588 and K5588 model combinations deviate, on average, by 47%, 17%, and 14%, respectively. Similarly, for the ^{66}Zn(α, γ)^{70}Ge reaction, the calculations using the K5188 (best χ^2), K6193, J5588, and K5588 model combinations deviate from the experimental data by 12%, 100%, 24%, and 25%, respectively.

In panels (c) and (d) of Fig. 7, we also compare the S factors reported by Gy. Gyürky et al. [45] for the ^{64}Zn(α, p)^{67}Ga and ^{64}Zn(α, n)^{67}Ge reactions, respectively, with those derived from TALYS−2.0 using the same model combinations –K5593, K6193, J5588, and K5588– that were used to calculate the S factors for the (α, γ) reaction on the same target nucleus. According to the relevant F_{rms} values, in the case of the former reaction, the K5593, K6193, J5588, and K5588 calculations deviate from the experimental S factors by 57%, 60%, 70%, and 54%, respectively. However, it is worth noting the large "scattering" of the experimental data below ≈8 MeV, which prevents any reliable conclusion on the best goodness-of-fit estimator. Similar arguments apply to the ^{64}Zn(α, n)^{67}Ge reaction, for which the reported S factor at 9.04 ± 0.08 MeV (almost at the opening of the (α, n) channel at 8.992 MeV) appears to be almost two orders of magnitude higher than the expected value. In this case, the F_{rms} values for the K5593, K6193, J5588, and K5588 calculations indicate deviations of 63%, 62%, 79% and 63%, respectively.

The TALYS−2.0 calculations for the ^{68}Zn(α, γ)^{72}Ge reaction are compared with our experimental data in Fig. 9. Panels (a) and (b) show the measured cross sections σ_g and σ_m to the ground and metastable states, respectively, while panel (c) displays their sum, i.e., the total reaction cross section σ_T. The corresponding astrophysical S factors, S_g, S_m, and S_T, are plotted in panels (d), (e), and (f), respectively. The TALYS−2.0 model combinations are indicated by the different types of curves in the legend. The black-filled circles represent the results obtained using the target with a thickness of $\xi = 625(32)$ μg/cm^2, while the open circles show the results from measurements with the 538(30)-μg/cm^2-thick target. As indicated by the gray bars in panels (c) and (f), the

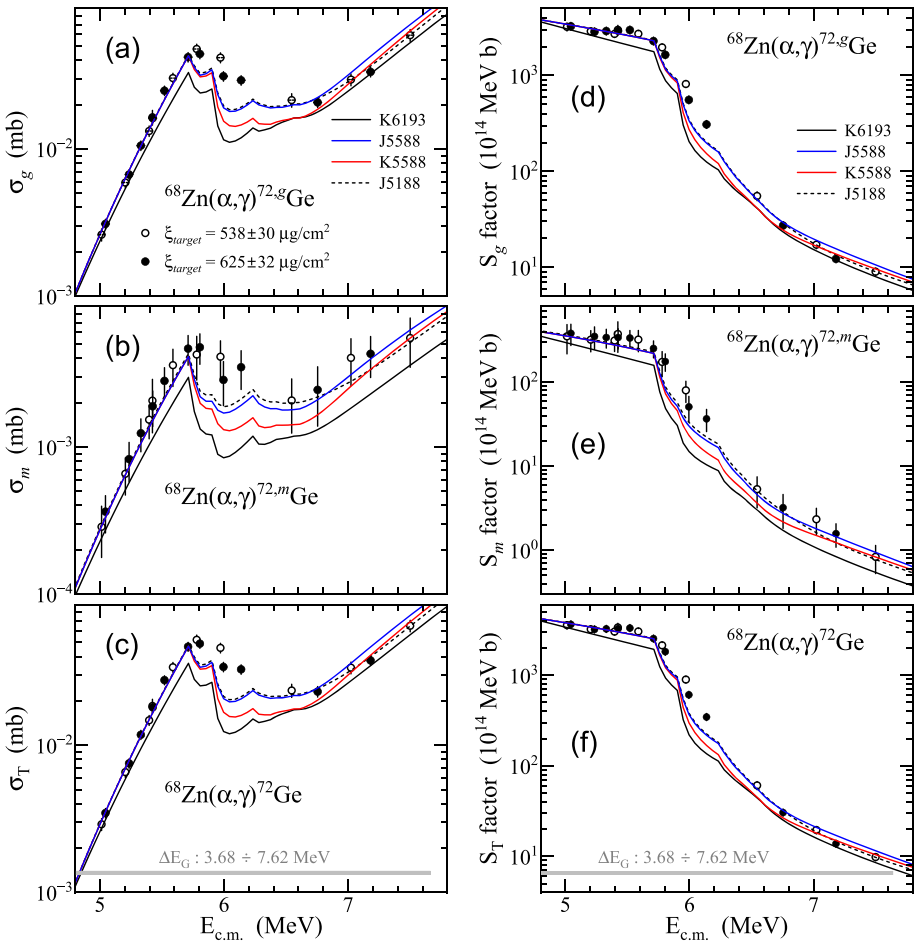

Fig. 9 Panels (**a**) and (**b**): Comparison of the measured cross sections to the ground state of ^{72}Ge, σ_g, and to its isomeric state, σ_m, with the predictions of TALYS−2.0 model combinations, as indicated by the different types of curves in the legend. The corresponding S factors are plotted in panels (**d**) and (**e**). The total cross section σ_T and the S factor S_T shown in panels (**c**) and (**f**), respectively, are the resulting total cross sections and the corresponding astrophysical S factors (see also text)

relevant Gamow energy region spans from 3.68 to 7.62 MeV, which means that, as in the previous cases, all our experimental data fall within this energy window.

The black dotted curves correspond to the TALYS−2.0 calculations with the best χ^2 are obtained using the model combination J5188, which combines the semi-microscopic *p*/*n*-OMP of Bauge, Delaroche, and Girod [33, 34] with the global semi-microscopic dispersive α-OMP/III of Demetriou et al. [36], the TALYS-specific CTFG NLD model, and the HFB/T/QRPA/G PSF for both $E1$ and $M1$ γ transitions. In all three cases, the J5588 combination appears to be the best when compared to the K5588 and, especially, the K6193 combinations. Indeed, when testing all four combinations using the F_{rms} values, the average deviations from the experimental data for the case of σ_g are 23%, 55%, 25%, and 35% for the corresponding TALYS−2.0 calculations using the J5188, K6193, J5588, and K5588 model combinations, respectively. Almost equal deviations were found for σ_m and σ_T.

The meta-to-ground cross-section ratios derived from panels (a) and (b) of Fig. 9 are compared in Fig. 10 with the corresponding calculations obtained using the four model combinations mentioned above. According to this figure, the meta-to-ground cross-section ratios obtained with the K6193 model combination show the largest deviation from the experimental data. However, since the relative errors of the experimental data points are quite large, ranging from 24 to 44%, no definitive conclusion can be drawn regarding the best model combination for their description.

Based on the above findings, one could argue that combinations using either the SMLO or HFB/T/QRPA/G PSF models, paired with either the TALYS-specific phenomenological CTFG or the microscopic HFB/Sk NLDs, can reproduce the experimental data with high accuracy. This holds true when they are combined with the semi-microscopic OMP/III α-OMP, but not with the phenomenological Avr/I α-OMP, regardless of whether they are paired with the phenomenological KD or the semi-microscopic JLM/B *p*/*n*-OMPs. To support this argument and draw final conclusions, however, it is essential to further validate the PSFs and NLDs and assess their contributions to the cross-section curves calculated with TALYS. These tasks are presented in the following subsections.

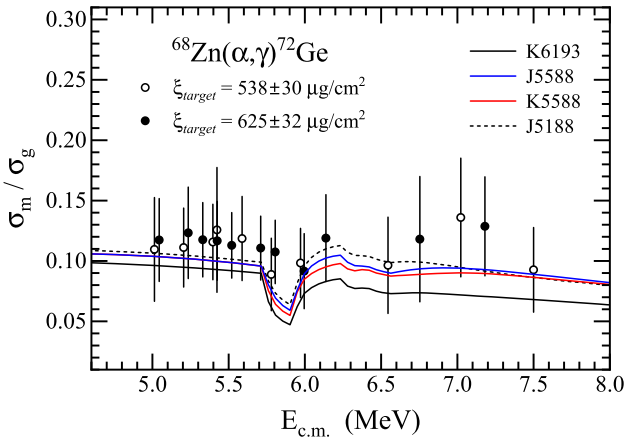

Fig. 10 Meta-to-ground cross-section ratios σ_m/σ_g determined in the present work for the ^{68}Zn(α, γ)^{72}Ge reaction

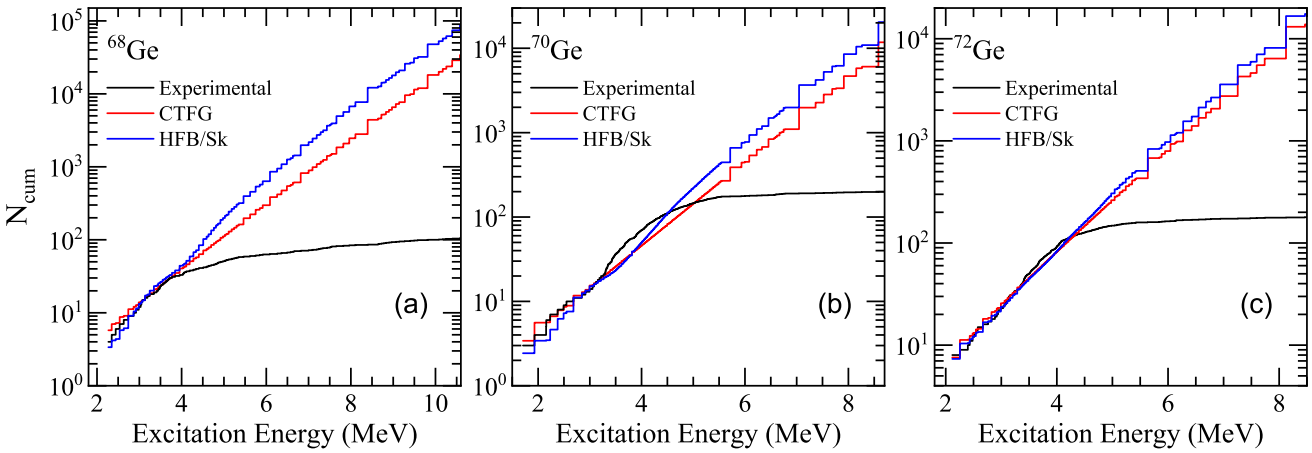

Fig. 11 Panel (**a**): Comparison of the cumulative number N_{cum} of low-lying levels observed in ^{68}Ge with the corresponding predictions of the two NLD models used in our TALYS calculations. Panels (**b**) and (**c**): Same as in panel (a) but for the ^{70}Ge and ^{72}Ge nuclei, respectively

5.2 Nuclear level densities (NLDs) and photostrength functions (PSFs)

Key nuclear quantities that can be used for comparison with the corresponding predictions of the NLD models applied in our calculations to validate them are the *s*-wave resonance spacings D_0 measured for the produced compound nuclei ^{68}Ge, ^{70}Ge, and ^{72}Ge, as well as the cumulative number N_{cum} of their excited levels with energies around or below their neutron separation energies. Experimental data on total radiative widths 0_γ could also serve to test the corresponding predictions of the TALYS calculations, although 0_γ is an integral over the NLD and the PSF and therefore depends on both the NLD and PSF models used to calculate them.

Due to the lack of experimental data on *s*-wave resonance spacings D_0 and radiative widths 0_γ for ^{68}Ge, ^{70}Ge, and ^{72}Ge nuclei, we compare in Fig. 11 their experimental cumulative numbers N_{cum} with the corresponding N_{cum} calculated using the two NLD models, CTFG and HFB/Sk. Their predictions are shown in Fig. 11 by curves with different colors, as indicated in the legends.

As can be seen in all three panels of Fig. 11, both NLD models used in our calculations successfully reproduce the low-energy part of the available phase space in all three produced compound nuclei. However, the experimental cumulative numbers shown in Fig. 11 correspond to excited levels with energies up to ≈11.8, 8.9, and 8.5 MeV for the ^{68}Ge, ^{70}Ge, and ^{72}Ge nuclei, respectively, whereas the energies of the levels populated in our measurements, as indicated by the E_{Σ_0} values in Tables 2, 3, and 4, are significantly higher.

Unfortunately, due to the lack of experimental data on D_0 for the produced compound nuclei, a meaningful comparison of the NLD models used in this work is not possible at excitation energies near the neutron separation energies S_n of ^{68}Ge (S_n = 12.392 MeV), ^{70}Ge (S_n = 11.533 MeV), and ^{72}Ge (S_n = 10.751 MeV), which are more relevant to the compound nucleus reactions studied here. The only existing experimental data on D_0 of indirect relevance to the reactions investigated is that for the ^{68}Zn target nucleus, which is 400 ± 60 eV. This value is excellently predicted by both NLDs: the CTFG NLD predicts a theoretical value of 399.77 eV, while the HFB/Sk NLD predicts 398.88 eV.

The two PSF models used in our calculations could be validated by comparing their predictions with experimentally determined PSFs. According to the recently updated PSF database [48, 49], experimental PSF data for $E1$ γ transitions are available only for

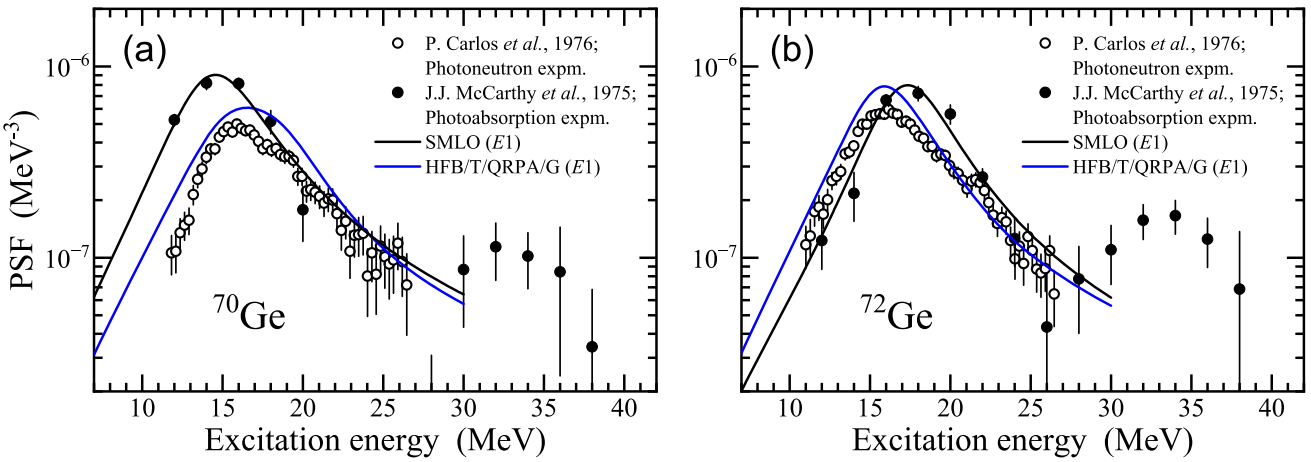

Fig. 12 Panel (**a**): Comparison of total PSF for $E1$ γ measured for ^{70}Ge with the corresponding predictions of the two PSF models used in TALYS calculations. Panel (**b**): same as in panel (**a**) but for the ^{72}Ge nucleus (see also text)

^{70}Ge and ^{72}Ge. These data were first reported by J. J. McCarthy et al. [50], who conducted a photoemission experiment, and by P. Carlos et al. [51], who carried out a photoneutron experiment. Their results are compared with the predictions of the SMLO and HFB/T/QRPA/G PSF models in Fig. 12.

As shown in this figure, the two publications mentioned above report different energy distributions for the first component of the Giant Dipole Resonance (GDR) in both nuclei. In the case of ^{70}Ge, for example, J. J. McCarthy et al. [50] found the first GDR peak at ≈15 MeV, whereas P. Carlos et al. [51] reported this peak at ≈16 MeV. On the other hand, the SMLO predictions are in excellent agreement with the $E1$ PSF data measured in the photoabsorption experiment [50]. In contrast, the HFB/T/QRPA/G PSF model appears to overestimate the data from the photoneutron experiment [51] and deviates significantly from the photoabsorption data.

Given the plots in Fig. 12, it is clear that the success of each PSF model depends on which of the two aforementioned experiments is regarded as the most credible. Possible explanations for the observed deviations between the two sets of PDR data, which could help in selecting the best PSF model for our TALYS calculations, may be found by assessing the different experimental approaches used by the authors of [50] and [51]. However, this task is beyond the scope of this paper. Since both PSF models used in our TALYS calculations are global models, their success may vary from nucleus to nucleus across the mass region to which they are applied. Thus, we regard both models as equally important for our TALYS calculations.

5.3 Alpha-nucleus optical model potentials (α-OMPs)

The differences between the NLD and PSF models discussed in the last two subsections are embedded in the varying predictions from the different combinations used in our calculations, shown in Figs. 7, 8, and 9. Therefore, before drawing final conclusions, it is important to identify the energies where these differences are significant– a task that is not straightforward given the theoretical curves resulting from combinations of models. This is particularly crucial for evaluating the predictive power of the two global α-OMPs used in this work.

In this context, an attempt was made to assess the contributions of the different models used in our TALYS calculations to the resulting cross-section curves by calculating cross-section ratios from model combinations that differ only in the choice of p/n-OMP, α-OMP, NLD, or PSF model. The resulting ratios are shown in panels (a), (b), and (c) of Fig. 13 for the ^{64}Zn(α, γ)^{68}Ge, ^{66}Zn(α, γ)^{70}Ge, and ^{68}Zn(α, γ)^{72}Ge reactions, respectively. In each panel, four cross-section ratios are plotted in different colors, corresponding to the model combinations indicated in the legend.

In addition to the colored curves shown in these panels, we also plot circles along the gray straight line corresponding to a cross-section ratio of 1. The position of the circles indicates the center-of-mass energies where cross sections were measured, and their gray bars represent the relative uncertainties of the corresponding data (see also Figs. 7, 8, and 9). The blue curve in panel (a) corresponds to the cross-section ratio obtained by dividing the cross sections calculated with the K6193 combination by those calculated with the K5193 model combination. This ratio depends only on the α-OMP, and as the blue curve shows, the Avr/I α-OMP by V. Avrigeanu et al. [35] differs significantly from the αOMP/III by Demetriou et al. [36], becoming very large – ranging from ≈50% to ≈100% – in the energy region between 6 and 4 MeV.

Similarly, the red curve in panel (a) corresponds to the ratio of cross sections obtained from the model combination K6193/K6593, indicating the differences in the cross sections due to the NLD. According to this curve, larger cross sections are obtained when using the HFB/Sk NLD model [38, 39] instead of the CTFG model [31]. The difference in cross sections at $E_{c.m.} \lessapprox 5.8$ MeV remains below 10%. The cross sections calculated with these two combinations are equal below 5 MeV, whereas at around 8.5 MeV, their difference becomes the largest.

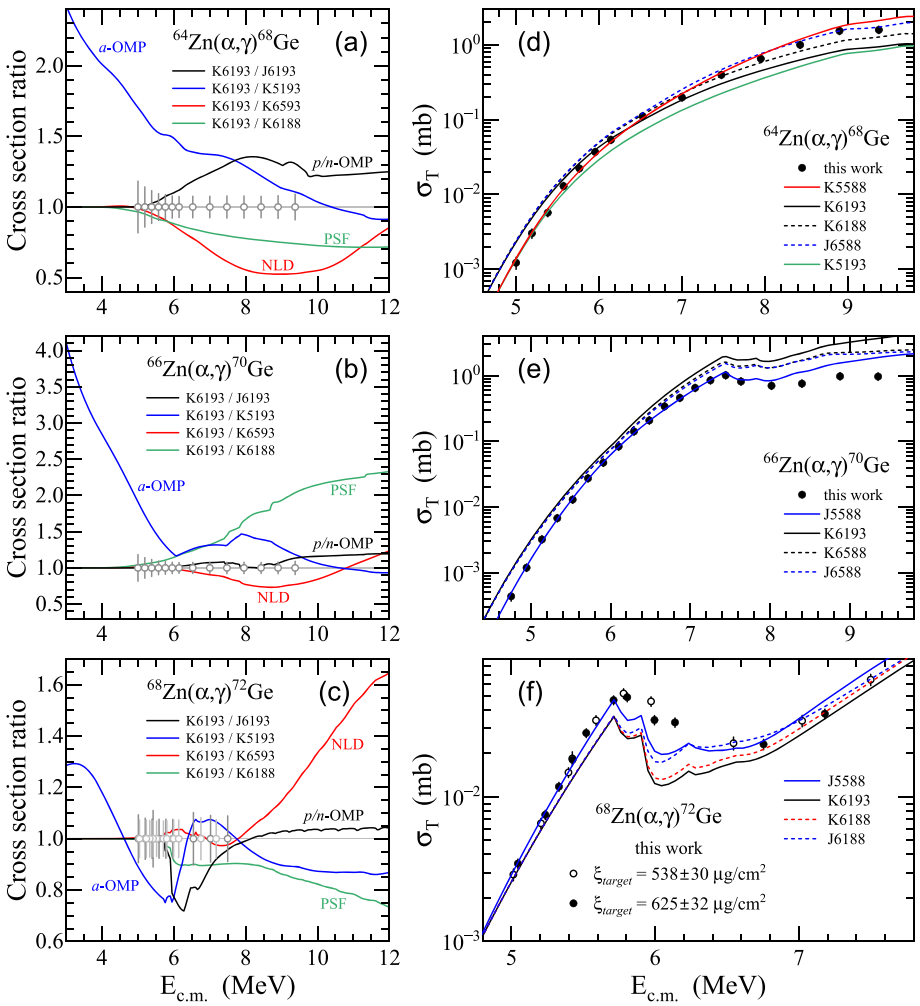

Fig. 13 Panels (**a**), (**b**) and (**c**): Cross-section ratios calculated for the ^{64}Zn(α, γ)^{68}Ge, ^{66}Zn(α, γ)^{70}Ge and ^{68}Zn(α, γ)^{72}Ge reactions, respectively. Panels (**d**), (**e**) and (**f**) show a comparison of the corresponding experimentally determined cross sections with the predictions of different model combinations also indicated by the legend (see text)

The green curve in panel (a) corresponds to the cross-section ratios obtained by dividing the cross sections calculated with the K6193 model combination by those calculated with K6188. Therefore, it indicates the energy region where the PSF models deviate the most. Again, the ratio deviates from unity at energies higher than ≈4.2 MeV but remains below 10% up to $E_{c.m.} \approx 5.5$ MeV. At higher energies, the ratio decreases continuously. According to the green curve, TALYS−2.0 calculations using the HFB/T/QRPA/G PSF model [31, 43, 44] provide, overall, larger cross sections compared to those obtained with the SMLO PSF model [40–42].

Finally, the black curve in panel (a), which depends on the *p*/*n*-OMP as it was obtained from the model combination ratio K6193/J6193, indicates an unexpected increase of up to ≈40% (around $E_{c.m.} \approx 8$ MeV), while remaining below the value of 1.1 at $E_{c.m.} \lessapprox 5.5$ MeV.

Given the above analysis, we can conclude that the cross sections of the ^{64}Zn(α, γ)^{68}Ge reaction, which were measured at $E_{c.m.} \lessapprox 5.5$ MeV, are almost independent of the *p*/*n*-OMP, NLD, and PSF, but are almost entirely dependent on the α-OMP. Moreover, the relative errors indicated by the gray bars on the circles plotted in panel (a) clearly show that the cross-section data measured up to $E_{c.m.} \lessapprox 5.5$ MeV are sensitive enough to allow for final conclusions about which α-OMP model best reproduces the experimental data. In this case, the best predictions are provided by the semi-microscopic α-OMP/III model by Demetriou et al. [36].

This conclusion is further confirmed by the cross-section calculations shown in panel (d) of Fig. 13. The black curve here corresponds to the cross sections calculated using the K6193 model combination (also shown in panel (a) of Fig. 7). This curve overestimates the experimental data up to ≈6.5 MeV. This behavior reverses at higher energies, and the deviation of the curve from the data increases continuously.

According to panel (a), a model combination using the α-OMP by V. Avrigeanu et al. [35], the CTFG or HFB/Sk NLD, and the HFB/T/QRPA/G PSF might be able to deliver higher cross sections at energies above 7 MeV. Indeed, in this energy region, as indicated by the curves corresponding to the K6188 and J6588 model combinations, the cross sections calculated with these combinations are higher than those obtained with K6193. However, none of these combinations provides cross sections smaller than those calculated with the K6193 combination at energies below ≈5.5 MeV. To achieve this, a combination using the semi-microscopic α-OMP/III by Demetriou et al. [36] is necessary.

Final conclusions on the α-OMP that best reproduces the experimental data for the other two reactions can be drawn from a similar analysis of the cross-section ratios shown in panels (b) and (c), along with the corresponding cross-section plots in panels (e) and (f). In these cases as well, the α-OMP/III by Demetriou et al. [36] best reproduces the data.

5.4 Reaction rates

Equally important for the evaluation of the discrepancies observed between the TALYS calculations and their deviations (either smaller or larger) from the experimental cross sections, shown in Figs. 7, 8, and 9, is the assessment of the resulting different reaction rates. The latter are key input parameters in the abundance calculations of *p*-nuclei.

For such an assessment, for each reaction studied in this work, we used the stellar reaction ratios obtained by dividing the stellar rates calculated with the three model combinations of interest, i.e., K6193, K5588, and J5588, by those calculated with the combination that best reproduces the corresponding experimental cross sections. All calculated stellar rates are given in Table 6.

As shown in Fig. 7 and already discussed in subsection 5.1, the model combination that best reproduces the corresponding experimental cross sections of the ^{64}Zn(α, γ)^{68}Ge reaction is K5593. For the ^{66}Zn(α, γ)^{70}Ge reaction, it is the K5188 model combination, whereas for ^{68}Zn(α, γ)^{72}Ge, it is the J5188. These three model combinations were selected because their predictions deviate the least from the experimental cross sections, which lie within the Gamow window for all reactions studied here. As such, they are the most suitable for calculating the rates of the nuclear reactions studied in this work.

The reaction-rate ratios, obtained as described above for different stellar temperatures, are plotted in panels (a), (b), and (c) of Fig. 14. In each panel, three curves of different colors are shown, representing the ratios indicated in the legend. Additionally, the gray vertical lines at T=2×10^9 *K* and T=3×10^9 *K* indicate the typical temperature range for the *p*-process. According to panel (a), in the case of the ^{64}Zn(α, γ)^{68}Ge reaction, the model combination that deviates the most from K5188 is the K6193 combination, which is the default combination in TALYS−2.0. Within the *p*-process relevant temperature range, it deviates by 70% to 100% from the reaction rates that best describe the experimental results. The other two combinations, K5588 and J5588, deviate from K5593 by no more than 5% within the relevant temperature range for the *p*-process.

In the case of the ^{66}Zn(α, γ)^{70}Ge reaction, shown in panel (b), the K6193 model combination deviates even more, between 70% and 130%, while the deviations of the other two combinations, K5588 and J5588, are almost negligible. The same applies to the ^{68}Zn(α, γ)^{72}Ge reaction shown in panel (c). Here, the J6193 model combination still deviates from the reaction rates that best describe the experimental results (J5188), but to a significantly lesser extent, between 10% and 15%.

Figure 14 includes three additional panels: (d), (e), and (f). In these panels, we plot the ratio of the reaction rates obtained from the two well-established reaction rate databases, BRUSLIB [52] and REACLIB [53], over those calculated using the semi-microscopic model combination J5588.

According to these panels, the BRUSLIB reaction rates deviate the most in the cases of the ^{64}Zn(α, γ)^{68}Ge and ^{66}Zn(α, γ)^{70}Ge reactions. Within the *p*-process relevant temperature range, they deviate by factors of $\approx$ 4 to 7 and 3 to 6, respectively. In contrast, the deviation for the ^{68}Zn(α, γ)^{72}Ge reaction is less than 10%. The REACLIB reaction rates also deviate in all three panels, but in the cases of the ^{64}Zn(α, γ)^{68}Ge and ^{68}Zn(α, γ)^{72}Ge reactions, the deviations are smaller than those of BRUSLIB. Finally, in the case of ^{68}Zn(α, γ)^{72}Ge, the REACLIB rates deviate by approximately 60% to 100%, significantly more than the BRUSLIB ratios.

6 Summary and conclusions

This paper reports on cross-section measurements of (α, γ) reactions on ^{64}Zn, ^{66}Zn, and ^{68}Zn at energies relevant to *p*-process nucleosynthesis, all within the corresponding Gamow energy windows, using the 4π γ-summing method [1, 8]. Through a comprehensive "in-out" analysis [1] of the current set of three and 12 previous cross-section measurements of (p, γ) and (α, γ) reactions, the relative errors in the absolute efficiency of the employed large-volume NaI(Tl) γ-summing detector were reduced to the 4% level, enabling a sensitive test of the cross-section predictions from statistical model calculations performed with the latest version (2.0) of the widely used TALYS code.

This test was implemented by comparing the experimentally determined cross sections with those calculated using certain combinations of global *p*/*n*-OMP, α-OMP, NLD an PSF models incorporated in the TALYS code. In particular, these calculations were performed with the combination used by default by TALYS, abbreviated as K6193, the semi-microscopic combination J5588 and the K5588.

The first model combination is purely phenomenological and combines the global *p*/*n*-OMP of Koning and Delaroche [32], the global α-OMP developed by V. Avrigeanu et al. [35], the TALYS-specific version of the Constant Temperature Fermi-Gas NLD model [31], and the Simple Modified Lorentzian (SMLO) model of PSF [40–42]. The second combination is semi-microscopic, combining the Lane-consistent *p*/*n*-OMP of Bauge, Delaroche, and Girod [33, 34], the semi-microscopic dispersive α-OMP of Demetriou et al. [36], the NLDs derived from a combinatorial method using nuclear structure properties determined with the Hartree-Fock-Bogolyubov (HFB) model and the BSk14 Skyrme force [38, 39], and the PSFs obtained from temperature-dependent HFB plus QRPA calculations using the D1M Gogny force [31, 43, 44]. The K5588 combination differs from the second one only in the *p*/*n*-OMP, which in this case is that of Koning and Delaroche [32].

Table 6 Stellar reaction rates calculated for the reactions studied in the present work using the model combinations listed in the 3rd row

T	^{64}Zn(α, γ)^{68}Ge				^{66}Zn(α, γ)^{70}Ge				^{68}Zn(α, γ)^{72}Ge			
($10^9 K$)	$N_A\langle\sigma\upsilon\rangle$ ($cm^3 s^{-1} mol^{-1}$)				$N_A\langle\sigma\upsilon\rangle$ ($cm^3 s^{-1} mol^{-1}$)				$N_A\langle\sigma\upsilon\rangle$ ($cm^3 s^{-1} mol^{-1}$)			
	K6193	J5588	K5588	K5593	K6193	J5588	K5588	K5188	K6193	J5588	K5588	J5188
0.3	6.1514E−40	1.6639E−40	1.6639E−40	1.6639E−40	8.3891E−40	9.4889E−41	9.4890E−41	9.4890E−41	9.5829E−40	6.3459E−39	6.3459E−39	6.3459E−39
0.4	2.8102E−32	7.7421E−33	7.7421E−E−33	7.7421E−33	3.4099E−32	3.9930E−33	3.9930E−33	3.9930E−33	3.9483E−32	7.2566E−32	7.2566E−32	7.2566E−32
0.5	1.4391E−27	4.1216E−28	4.1216E−28	4.1216E−28	1.6609E−27	2.0960E−28	2.0960E−28	2.0960E−28	1.9514E−27	2.0478E−27	2.0478E−27	2.0478E−27
0.6	2.8895E−24	8.7742E−25	8.7742E−25	8.7742E−25	3.3003E−24	4.6675E−25	4.6675E−25	4.6675E−25	3.9447E−24	3.3909E−24	3.3909E−24	3.3909E−24
0.7	9.8634E−22	3.2067E−22	3.2067E−22	3.2067E−22	1.1393E−21	1.8388E−22	1.8388E−22	1.8388E−22	1.3849E−21	1.1257E−21	1.1257E−21	1.1257E−21
0.8	1.1198E−19	3.8973E−20	3.8973E−20	3.8973E−20	1.3205E−19	2.4260E−20	2.4260E−20	2.4260E−20	1.6238E−19	1.2980E−19	1.2980E−19	1.2980E−19
0.9	5.9573E−18	2.2101E−18	2.2101E−18	2.2101E−18	7.1994E−18	1.4891E−18	1.4891E−18	1.4891E−18	8.8786E−18	7.0366E−18	7.0366E−18	7.0366E−18
1	1.8144E−16	7.1289E−17	7.1289E−17	7.1289E−17	2.2480E−16	5.1634E−17	5.1634E−17	5.1634E−17	2.7526E−16	2.1704E−16	2.1704E−16	2.1704E−16
1.5	3.0631E−11	1.4445E−11	1.4438E−11	1.4437E−11	4.0683E−11	1.3401E−11	1.3399E−11	1.3403E−11	4.3193E−11	3.5885E−11	3.5885E−11	3.5888E−11
2	5.5280E−08	2.8800E−08	2.8455E−08	2.8576E−08	7.2200E−08	3.0888E−08	3.0815E−08	3.0889E−08	6.4223E−08	6.1285E−08	6.1316E−08	6.1359E−08
2.5	9.3930E−06	5.3692E−06	5.1293E−06	5.2309E−06	1.2583E−05	6.6243E−06	6.5441E−06	6.5938E−06	9.0929E−06	9.6945E−06	9.7226E−06	9.7416E−06
3	3.7235E−04	2.3368E−04	2.1386E−04	2.2244E−04	5.6139E−04	3.3616E−04	3.2659E−04	3.3094E−04	3.0179E−04	3.4238E−04	3.4485E−04	3.4598E−04
3.5	5.7233E−03	3.9382E−03	3.4606E−03	3.6628E−03	1.0202E−02	6.4980E−03	6.2038E−03	6.3049E−03	3.8639E−03	4.5278E−03	4.5853E−03	4.6077E−03
4	4.6257E−02	3.4830E−02	2.9552E−02	3.1700E−02	9.7756E−02	6.3632E−02	5.9872E−02	6.0830E−02	2.5982E−02	3.0886E−02	3.1463E−02	3.1737E−02
5	8.6726E−01	7.6907E−01	6.1833E−01	6.7335E−01	2.4337E+00	1.5621E+00	1.4416E+00	1.4614E+00	3.4916E−01	4.0802E−01	4.2007E−01	4.3676E−01
6	5.6906E+00	5.6346E+00	4.3706E+00	4.7665E+00	1.9717E+01	1.1885E+01	1.0845E+01	1.1170E+01	1.8413E+00	1.9801E+00	2.0466E+00	2.3211E+00
7	1.9880E+01	2.0426E+01	1.5519E+01	1.6742E+01	8.0354E+01	4.3249E+01	3.9120E+01	4.2607E+01	6.0117E+00	5.7087E+00	5.8557E+00	7.6300E+00
8	4.7711E+01	4.7925E+01	3.6113E+01	3.8165E+01	2.1097E+02	9.7064E+01	8.6917E+01	1.0444E+02	1.4887E+01	1.2699E+01	1.2813E+01	1.9198E+01
9	9.1585E+01	8.6742E+01	6.5379E+01	6.7384E+01	4.1069E+02	1.5957E+02	1.4105E+02	1.9060E+02	2.9602E+01	2.4116E+01	2.3912E+01	3.9089E+01
10	1.5184E+02	1.3336E+02	1.0096E+02	1.0162E+02	6.4024E+02	2.1677E+02	1.8868E+02	2.8149E+02	4.7834E+01	4.0139E+01	3.9251E+01	6.4801E+01

The stellar temperatures T are given in the first column (see also text)

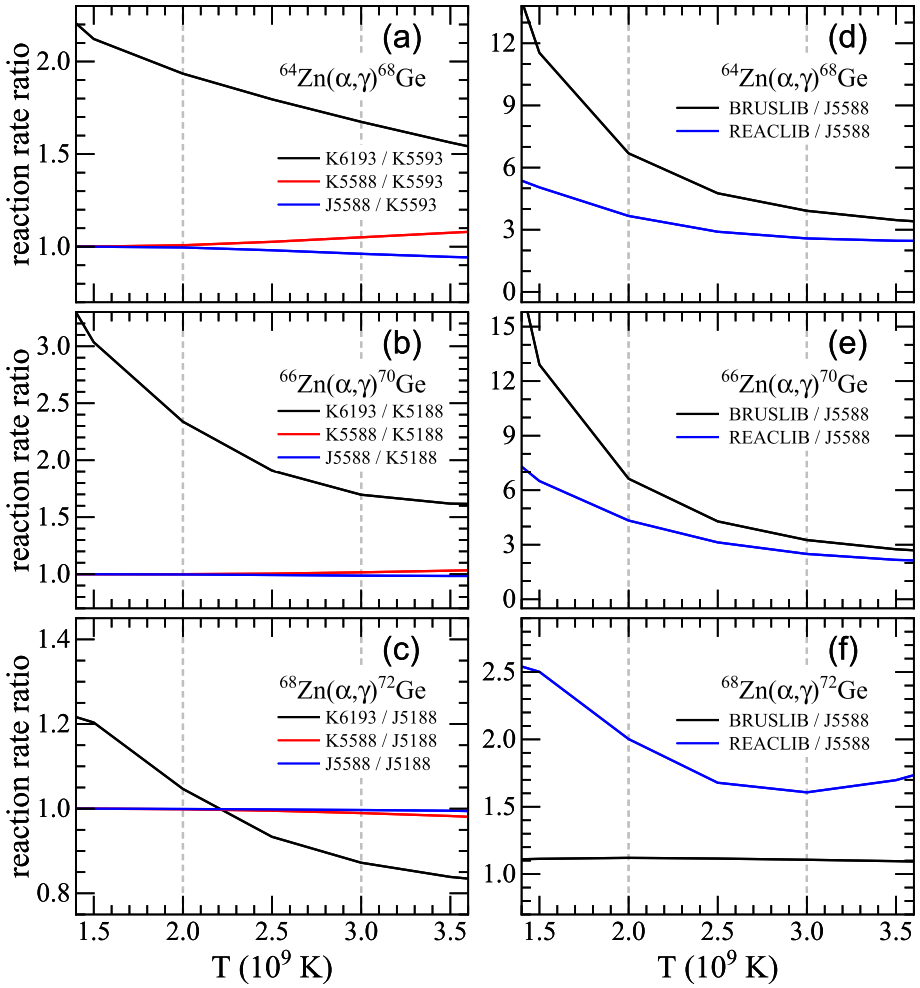

Fig. 14 Panels (**a**), (**b**), and (**c**): Reaction-rate ratios obtained for the nuclear reactions indicated in the legend by dividing the reaction rates calculated with the model combinations K6193, K5588, and J5588 by those calculated with the combinations that best reproduce the corresponding experimental cross sections, as shown in panels (**a**) of Figs. 7 and 8, and panel (**c**) of Fig. 9, respectively. The reaction-rate ratios plotted in panels (**d**), (**e**), and (**f**) were calculated by dividing the rates obtained from the BRUSLIB [52] and REACLIB [53] databases by those calculated using the semi-microscopic model combination J5588 (see also the text)

From the comparison of the experimental data with the TALYS−2.0 calculations, the following conclusions can be drawn:

- In all three cases of the investigated (α, γ) reactions, the experimental data can be successfully reproduced by exclusively using the α-OMP of Demetriou et al. [36], almost independently of the other nuclear models for the *p*/*n*-OMP, NLD, and PSF.
- Both the K5588 and the J5588 model combinations reproduce the experimental data almost equally well. This demonstrates that the predictive power of the semi-microscopic *p*/*n*-OMP of Bauge, Delaroche, and Girod [33, 34] is comparable to that of the well-established phenomenological *p*/*n*-OMP of Koning and Delaroche [32].
- The PSFs obtained from temperature-dependent HFB plus QRPA calculations using the D1M Gogny force [31, 43, 44] were found to successfully reproduce the experimental data of this work when combined with the α-OMP of Demetriou et al. [36] and the Skyrme HFB NLDs [38, 39]. The predictive power of this PSF model is equal to, if not exceeding, that of the phenomenological Simplified Modified Lorentzian (SMLO).
- Similar to our recent work on (p, γ) cross-section measurements on Sn isotopes [12], the Skyrme HFB NLD model [38, 39] was once again found to undeniably stand out as a "robust" NLD model, as suggested in [31].

Stellar reaction rates were also derived in the present work using the three model combinations K6193, J5588, and K5588. The results obtained with the latter two combinations were found to agree within 10% in the relevant temperature range for the *p*-process. Reaction rates calculated using the K6193 combination deviated from those of the other two by more than 70% for the ^{64}Zn(α, γ)^{68}Ge and ^{66}Zn(α, γ)^{70}Ge reactions, but by no more than 15% in the case of ^{68}Zn(α, γ)^{72}Ge.

The reaction rates obtained using the semi-microscopic model combination J5588 were compared with those from the BRUSLIB [52] and REACLIB [53] databases. It was found that the rates from the former database deviate strongly, by up to a factor of 7, within the temperature range relevant to the *p*-process for the ^{64}Zn(α, γ)^{68}Ge and ^{66}Zn(α, γ)^{70}Ge reactions, but by no more than 10% in the case of ^{68}Zn(α, γ)^{72}Ge. The reaction rates from the REACLIB database deviated less in the first two cases, whereas in the case of the latter reaction, they deviated more than the BRUSLIB rates, by a factor between 1.5 and 2.

It is worth noting that the final conclusions of this work cannot be considered applicable to all (α, γ) reactions on nuclei located not only in mass regions away from the present one but also close to it. As will be communicated in forthcoming papers, the level

of success of some of the models used in the present calculations in reproducing experimental data varies from that found in the present case.

The last important finding of this work is based on the blue curves plotted in panels (a) and (b) of Fig. 13, which clearly demonstrate that in order to test the predictions of the existing α-OMPs, we need to measure (α, γ) cross sections in many other reactions, notably at energies as low as possible, and cover the lower part of the corresponding Gamow windows.

Acknowledgements This work was supported by the Hellenic Foundation for Research and Innovation (H.F.R.I.) under the "2nd Call for H.F.R.I. Research Projects to support Faculty Members and Researchers" (Project Number: 4650/ARENA).

Funding Open access funding provided by HEAL-Link Greece.

Data Availability Statement Datasets generated during the current study are available from the corresponding author on reasonable request.

References

1. A. Spyrou, H.-W. Becker, A. Lagoyannis, S. Harissopulos, C. Rolfs, Cross-section measurements of capture reactions relevant to the p process using a 4 π gamma-summing method. Phys. Rev. C **76**, 015802 (2007). https://doi.org/10.1103/PhysRevC.76.015802
2. M. Arnould, S. Goriely, The p-process of stellar nucleosynthesis: astrophysics and nuclear physics status. Phys. Rep. **384**, 1 (2003). https://doi.org/10.1016/S0370-1573(03)00242-4
3. T. Rauscher, N. Dauphas, I. Dillmann, C. Fröhlich, Zs Fülöp and Gy Gyürky, Constraining the astrophysical origin of the p-nuclei through nuclear physics and meteoritic data. Rep. Prog. Phys. **76**, 066201 (2013). https://doi.org/10.1088/0034-4885/76/6/066201
4. M. Pignatari, K. Göbel, R. Reifarth, C. Travaglio, The production of proton-rich isotopes beyond iron: the γ-process in stars. Int. J. Mod. Phys. E **25**, 1630003 (2016). https://doi.org/10.1142/S0218301316300034
5. P. Tsagari, M. Kokkoris, E. Skreti, A.G. Karydas, S. Harissopulos, T. Paradellis, P. Demetriou, Cross section measurements of the ^{89}Y$(p, \gamma)^{90}$Zr reaction at energies relevant to p-process nucleosynthesis. Phys. Rev. C **70**, 015802 (2004). https://doi.org/10.1103/PhysRevC.70.015802
6. A. Spyrou, A. Lagoyannis, P. Demetriou, S. Harissopulos, H.-W. Becker, Cross section measurements of (p, γ) reactions on Pd isotopes relevant to the p process. Phys. Rev. C **77**, 065801 (2008). https://doi.org/10.1103/PhysRevC.77.065801
7. S. Harissopulos, A. Spyrou, A. Lagoyannis, M. Axiotis, P. Demetriou, J.W. Hammer, R. Kunz, H.-W. Becker, Cross section measurements of proton capture reactions relevant to the p process: the case of ^{89}Y$(p, \gamma)^{90}$Zr and ^{121,123}Sb$(p, \gamma)^{122,124}$Te. Phys. Rev. C **87**, 025806 (2013). https://doi.org/10.1103/PhysRevC.87.025806
8. V. Sotirios, Harissopulos, Cross-section measurements of capture reactions relevant to p-process nucleosynthesis. Eur. Phys. J. Plus **133**, 332 (2018). https://doi.org/10.1140/epjp/i2018-12185-8
9. V. Foteinou, M. Axiotis, S. Harissopulos, P. Dimitriou, G. Provatas, A. Lagoyannis, H.-W. Becker, D. Rogalla, A. Zilges, A. Schreckling, A. Endres, Cross section measurements of proton capture reactions on Mo isotopes relevant to the astrophysical p process. Eur. Phys. J. A **55**, 67 (2019). https://doi.org/10.1140/epja/i2019-12738-x
10. S. Harissopulos, Eleni Vagena, M. Axiotis, A. Spyrou, G. Provatas, A. Lagoyannis, P. Dimitriou, Capture reaction cross-section measurements relevant to p process: the case of (α, γ) reactions on ^{63}Cu, ^{72}Ge, ^{118}Sn and the ^{107}Ag$(p, \gamma)^{108}$Cd reaction. EPJ Web Conf. **227**, 0100 (2020). https://doi.org/10.1051/epjconf/202022701008
11. S. Harissopulos, E. Vagena, P. Dimitriou, M. Axiotis, S. Galanopoulos, V. Foteinou, A. Lagoyannis, Cross section measurements of proton capture reactions on Sr isotopes for astrophysics applications. Phys. Rev. C **104**, 025804 (2021). https://doi.org/10.1103/PhysRevC.104.025804
12. S. Harissopulos, E. Vagena, A. Spyrou, M. Axiotis, Z. Kotsina, K. Tsampa, A. Lagoyannis, P. Dimitriou, H.-W. Becker, V. Foteinou, (p, γ) cross section measurements on Sn isotopes relevant to the p process. Phys. Rev. C **110**, 015803 (2024). https://doi.org/10.1103/PhysRevC.110.015803
13. A. Simon, S.J. Quinn, A. Spyrou, A. Battaglia, I. Beskin, A. Best, B. Bucher, M. Couder, P.A. DeYoung, X. Fang, J. Görres, A. Kontos, Q. Li, S.N. Liddick, A. Long, S. Lyons, K. Padmanabhan, J. Peace, A. Roberts, D. Robertson, K. Smith, M.K. Smith, E. Stech, B. Stefanek, W.P. Tan, X.D. Tang, Summing NaI(Tl) gamma-ray detector for capture reaction measurements. Nucl. Instr. Meth. Phys. Res. A **703**, 16 (2013). https://doi.org/10.1016/j.nima.2012.11.045
14. C.S. Reingold, O. Olivas-Gomez, A. Simon, J. Arroyo, M. Chamberlain, J. Wurzer, A. Spyrou, F. Naqvi, A.C. Dombos, A. Palmisano, T. Anderson, A.M. Clark, B. Frentz, M.R. Hall, S.L. Henderson, S. Moylan, D. Robertson, M. Skulski, E. Stech, S.Y. Strauss, W.P. Tan, B. Vande Kolk, High efficiency total absorption spectrometer HECTOR for capture reaction measurements. Eur. Phys. J. A **55**, 77 (2019). https://doi.org/10.1140/epja/i2019-12748-8
15. W. Hauser, H. Feshbach, The inelastic scattering of neutrons. Phys. Rev. **87**, 366 (1952). https://doi.org/10.1103/PhysRev.87.366
16. T. Rauscher, N. Nishimura, R. Hirschi, G. Cescutti, A. St, J. Murphy, A. Heger, Uncertainties in the production of p nuclei in massive stars obtained from Monte Carlo variations. Mon. Not. R. Astron. Soc. **463**, 4153 (2016). https://doi.org/10.1093/mnras/stw2266
17. N. Nishimura, T. Rauscher, R. Hirschi, A. St, J. Murphy, G. Cescutti, C. Travaglio, Uncertainties in the production of p nuclides in thermonuclear supernovae determined by Monte Carlo variations. Mon. Not. R. Astron. Soc. **474**, 3133 (2018). https://doi.org/10.1093/mnras/stx3033
18. S. Goriely, W. Ryssens, S. Hilaire, S. Péru, Nuclear inputs relevant to nuclear astrophysics, status and perspectives. EPJ Web Conf. **322**, 09001 (2025). https://doi.org/10.1051/epjconf/202532209001
19. Y. Wang, M. Nastasi (eds.), *Handbook of Modern Ion Beam Materials Analysis* (Materials Research Society, Cambridge University Press, Cambridge, 2010)
20. V. Foteinou, F. Maragkos, H.-W. Becker, L. Hess, K. Ivanković, M. Kokkoris, M. Mayer, G. Provatas, D. Rogalla, Differential cross-section measurements for the ^{9}Be(^{3}He,^{3} He$_0$)^{9}Be elastic scattering and the ^{9}Be(^{3}He, p_x)^{11}B reactions. Nucl. Instum. Methods Phys. Res. B **542**, 158 (2023)

21. S. Harissopulos, M. Andrianis, M. Axiotis, A. Lagoyannis, A.G. Karydas, Z. Kotsina, A. Laoutaris, G. Apostolopoulos, A. Theodorou, T. Zouros, I. Madesis, E.P. Benis, The Tandem Accelerator Laboratory of NCSR "Demokritos": current status and perspectives. Eur. Phys. J. Plus **136**, 617 (2021). https://doi.org/10.1140/epjp/s13360-021-01596-5
22. M. Mayer, SIMNRA, a simulation program for the analysis of NRA, RBS and ERDA, Proceedings of the 15th International Conference on the Application of Accelerators in Research and Industry, J.L. Duggan and I.L. Morgan (eds.), AIP Conf. Proc. **475**, 541 (1999); https://doi.org/10.1063/1.59188
23. J.F. Ziegler, M.D. Ziegler, J.P. Biersack, SRIM - The stopping and range of ions in matter (2010), Nucl. Instr. Meth. Phys. Res. B **268**, 1818 (2010); https://doi.org/10.1016/j.nimb.2010.02.091, and James F. Ziegler, The Stopping and Range of Ions in Matter; Code SRIM (available online at http://www.srim.org/)
24. IAEA Live Chart of Nuclides, Nuclear Structure and Decay Data based on the Evaluated Nuclear Structure Data File (ENSDF), https://www-nds.iaea.org/livechart/
25. Gauri Datar, C. Geeta Vichare, A.B. Selvaraj, A. Raghav, Causes of the diurnal variation observed in gamma-ray spectrum using NaI (Tl) detector. J. Atmos. Sol.-Terr. Phys. **207**, 105369 (2020). https://doi.org/10.1016/j.jastp.2020.105369
26. J. Theuerkauf, S. Esser, S. Krink, M. Luig, N. Nicolay, O. Stuch and H. Wolters, Program Tv, Institute of Nuclear Physics, University of Cologne, (2000); https://apps.ikp.uni-koeln.de/~fitz/viewspectra/Tv_user-manual/
27. J. Mayer, E. Hoemann, O. Papst, N. Warr, N. Braun, T. Kotthaus and R. Schulze, HDTV - Nuclear Spectrum Analysis Tool, Institute of Nuclear Physics, University of Cologne, (2020); https://gitlab.ikp.uni-koeln.de/jmayer/hdtv
28. A. Markowicz, R.V. Grieken, *Handbook on X-Ray Spectrometry* (Marcel Dekker, New York, 1993)
29. W.J. Meng Wang, F.G. Huang, G. Kondev, S.N. Audi, The AME 2020 atomic mass evaluation (II). Chin. Phys. C **45**, 030003 (2021). https://doi.org/10.1088/1674-1137/abddaf
30. C. Iliadis, *Nuclear Physics of Stars* (Wiley-VCH Verlag, Weinheim, Germany, 2007)
31. A. Koning, S. Hilaire, S. Goriely, TALYS: modeling of nuclear reactions. Eur. Phys. J. A **59**, 131 (2023). https://doi.org/10.1140/epja/s10050-023-01034-3
32. A.J. Koning, J.P. Delaroche, Local and global nucleon optical models from 1 keV to 200 MeV. Nucl. Phys. A **713**, 231 (2003). https://doi.org/10.1016/S0375-9474(02)01321-0
33. E. Bauge, J.P. Delaroche, M. Girod, Lane-consistent, semimicroscopic nucleon-nucleus optical model. Phys. Rev. C **63**, 024607 (2001). https://doi.org/10.1103/PhysRevC.63.024607
34. E. Bauge, J.P. Delaroche, M. Girod, Semimicroscopic nucleon-nucleus spherical optical model for nuclei with A≥40 at energies up to 200 MeV. Phys. Rev. C **58**, 1118 (1998). https://doi.org/10.1103/PhysRevC.58.1118
35. V. Avrigeanu, M. Avrigeanu, C. Mănăilescu, Further explorations of the α-particle optical model potential at low energies for the mass range A≈45-209. Phys. Rev. C **90**, 044612 (2014). https://doi.org/10.1103/PhysRevC.90.044612
36. P. Demetriou, C. Grama, S. Goriely, Improved global α-optical model potentials at low energies. Nucl. Phys. A **707**, 253 (2002). https://doi.org/10.1016/S0375-9474(02)00756-X
37. A. Gilbert, A. Cameron, A composite nuclear-level density formula with shell corrections. Can. J. Phys. **43**, 1446 (1965). https://doi.org/10.1139/p65-139
38. S. Goriely, S. Hilaire, A.J. Koning, Improved microscopic nuclear level densities within the Hartree-Fock-Bogoliubov plus combinatorial method. Phys. Rev. C **78**, 064307 (2008). https://doi.org/10.1103/PhysRevC.78.064307
39. S. Hilaire, S. Goriely, Global microscopic nuclear level densities within the HFB plus combinatorial method for practical applications. Nucl. Phys. A **779**, 63 (2006)
40. V.A. Plujko, O.M. Gorbachenko, R. Capote, P. Dimitriou, Giant dipole resonance parameters of ground-state photoabsorption: Experimental values with uncertainties. At. Data Nucl. Data Tables **123**, 1 (2018). https://doi.org/10.1016/j.adt.2018.03.002
41. S. Goriely, V. Plujko, Simple emirical E1 and M1 strngth functions for practical applications. Phys. Rev. C **99**, 014303 (2019). https://doi.org/10.1103/PhysRevC.99.014303
42. S. Goriely, P. Dimitriou, M. Wiedeking, T. Belgya, R. Firestone, J. Kopecky, M. Krticka, V. Plujko, R. Schwengner, S. Siem, H. Utsunomiya, S. Hilaire, S. Peru, Y.S. Cho, D.M. Filipescu, N. Iwamoto, T. Kawano, V. Varlamov, R. Xu, Reference database for photon strength functions. Eur. Phys. J. A **55**, 172 (2019). https://doi.org/10.1140/epja/i2019-12840-1
43. S. Goriely, S. Hilaire Péru, K. Sieja, Gogny+HFB+QRPA dipole strength function and its application to radiative nucleon capture cross section. Phys. Rev. C **98**, 014327 (2018). https://doi.org/10.1103/PhysRevC.98.014327
44. M. Martini, S. Péru, S. Hilaire, S. Goriely, F. Lechaftois, Large-scale deformed quasiparticle random-phase approximation calculations of the γ-ray strength function using the Gogny force. Phys. Rev. C **94**, 014304 (2016). https://doi.org/10.1103/PhysRevC.94.014304
45. Gy. Gyürky, P. Mohr, Zs. Fülöp, Z. Halász, G. G. Kiss, T. Szücs, and E. Somorjai, Relation between total cross sections from elastic scattering and α-induced reactions: The example of ^{64}Zn, Phys. Rev. C **86**, 041601 (2012); https://doi.org/10.1103/PhysRevC.86.041601
46. A. Koning, TASMAN-2.0 Statistical software for TALYS: Uncertainties, sensitivities and optimization, 2023 https://nds.iaea.org/talys/tutorials/tasman.pdf
47. A.J. Koning, D. Rochman, J.-C. Sublet, N. Dzysiuk, M. Fleming, S. van der Marck, TENDL: complete nuclear data library for innovative nuclear science and technology. Nucl. Data Sheets **155**, 1 (2019). https://doi.org/10.1016/j.nds.2019.01.002
48. S. Goriely, P. Dimitriou, M. Wiedeking, T. Belgya, R. Firestone, J. Kopecky, M. Krtička, V. Plujko, R. Schwengner, S. Siem, H. Utsunomiya, S. Hilaire, S. Péru, Y. S. Cho, D. M. Filipescu, N. Iwamoto, T. Kawano, V. Varlamov, R. Xu, (2019) Reference database for photon strength functions. Eur. Phys. J. a **55**, 172 . https://doi.org/10.1140/epja/i2019-12840-1
49. IAEA Photon Strength Function Database; https://www-nds.iaea.org/PSFdatabase/
50. J.J. McCarthy, R.C. Morrison, H.J. Vandermolent, Systematic study of the photodisintegration of ^{70}Ge, ^{72}Ge, ^{74}Ge and ^{76}Ge. Phys. Rev. C **11**, 772 (1975). https://doi.org/10.1103/PhysRevC.11.772
51. P. Carlos, H. Beil, H. Bergère, J. Fagot, A. Leprêtre, A. Veyssière, G.V. Solodukhov, A study of the photoneutron contribution to the giant dipole resonance of nuclei in the 64 ≤ A ≤ 86 mass region. Nucl. Phys. A **258**, 365 (1976). https://doi.org/10.1016/0375-9474(76)90012-9
52. Y. Xu, S. Goriely, A. Jorissen, G.L. Chen, M. Arnould, Databases and tools for nuclear astrophysics applications: BRUSsels Nuclear LIBrary (BRUSLIB), Nuclear Astrophysics Compilation of REactions II (NACRE II) and Nuclear NETwork GENerator (NETGEN). Astron. Astrophys. **549**, A106 (2013). https://doi.org/10.1051/0004-6361/201220537
53. R.H. Cyburt, A.M. Amthor, R. Ferguson, Z. Meisel, K. Smith, S. Warren, A. Heger, R.D. Hoffman, T. Rauscher, A. Sakharuk, H. Schatz, F.K. Thielemann, M. Wiescher, The Jina reaclib database: its recent updates and impact on type-IX-ray bursts. Astrophys. J. Suppl. Ser. **189**, 240 (2010). https://doi.org/10.1088/0067-0049/189/1/240